2016

# Evaluation Of The Engine Exhaust Particle Sizer (eeps) For Real-Time Measurements Of Diesel And Biodiesel Exhaust Particulate Matter

James Robert Dunshee
*University of Vermont*

# EVALUATION OF THE ENGINE EXHAUST PARTICLE SIZER (EEPS) FOR REAL-TIME MEASUREMENTS OF DIESEL AND BIODIESEL EXHAUST PARTICULATE MATTER

A Thesis Presented

by

Jim Dunshee

to

The Faculty of the Graduate College

of

The University of Vermont

In Partial Fulfillment of the Requirements
for the Degree of Master of Science
Specializing in Civil and Environmental Engineering

May, 2016

Defense Date: November 11, 2015
Thesis Examination Committee:

Britt A. Holmén, Ph.D., Advisor
Giuseppe A. Petrucci, Ph.D., Chairperson
Appala Raju Badireddy, Ph.D.
Cynthia J. Forehand, Ph.D., Dean of the Graduate College

## ABSTRACT

Even at low concentrations, the criteria air pollutant particulate matter (PM) is an environmental and public health hazard. Emissions levels legislated for modern diesel vehicles are so low (~90% lower than 2003) that it has become difficult to accurately measure PM by the regulatory metric: the mass of particles collected on a filter (i.e., the gravimetric method). Additionally, gravimetric analysis cannot measure real-time emission rates, and therefore is unable to characterize high-emitting transient events (e.g., engine starts, stop-and-go driving). By an alternate method, PM can be estimated by measuring the number-weighted particle size distribution (PSD) and calculating mass with a combination of theoretical and empirical constants (e.g., particle effective density). This integrated particle size distribution (IPSD) method is capable of high measurement sensitivity and real-time resolution.

Real-time measurements by the IPSD method require fast-sizing spectrometers, such as the TSI Engine Exhaust Particle Sizer (EEPS), which sizes (between 5.6-560 nm) and counts particles based on their electrical mobility. The EEPS utilizes a unipolar charger to quickly charge particles for sizing and counting, however this mechanism has been shown to produce a less predictable charge distribution than bipolar chargers used in Scanning Mobility Particle Sizer (SMPS) systems – the gold standard "slow-sizing" spectrometer. Several evaluations have shown deficiencies in EEPS PSD measurements due to charging differences (associated with particle morphology) unaccounted for in the transfer function matrix used to calibrate the EEPS. Specifically, the unipolar charger multiply charges a higher percentage of soot agglomerates (fractal-like particles common in diesel engine exhaust) than bipolar chargers. Because inaccurate PSDs are a primary reason for reported discrepancies between IPSD calculated mass and the gravimetric method, it is important to correct this deficiency in EEPS measurements. Recently, TSI has released additional EEPS calibration matrices ("*Soot*" and "*Compact*") which have shown better agreement with SMPS measurements under preliminary test conditions. This study further evaluates the performance of these new matrices relative to the original "*Default*" matrix for diesel and biodiesel exhaust particles.

Steady-state (75% engine load) emissions were generated by a light-duty diesel engine operating on (1) ultra-low sulfur diesel (ULSD) and (2) 100% soybean biodiesel. Raw EEPS data processed with each matrix were compared to simultaneously collected reference measurements from an SMPS. PSDs were evaluated based on their shape – i.e., multimodal fits of geometric mean diameter (GMD) and geometric standard deviation (GSD) – and concentration at peak particle diameter. For both fuels, all measurements agreed well in terms of the shape of the PSD: primary mode (accumulation) GMD ± 10nm, GSD ± 0.3. For ULSD, EEPS *Default*, *Soot*, and *Compact* concentrations were higher than the SMPS by factors of 1.9, 1.3, and 2.5, respectively. For biodiesel, EEPS *Default*, *Soot*, and *Compact* concentrations were higher than the SMPS by factors of 2.1, 1.7, and 2.4, respectively. Based on these results, the *Soot* matrix produced acceptable agreement between EEPS and SMPS measurements of ULSD exhaust particles. However, based on the factor of ~2 difference observed here, an additional calibration matrix may be necessary for the EEPS to accurately measure biodiesel exhaust particles.

The IPSD method for estimating PM mass was applied to available data sets with corresponding gravimetric measurements (one ULSD transient cycle test and the same biodiesel steady-state test used for PSD evaluation). Real-time PSDs from each of the three EEPS matrices were used in combination with three sets of values assumed for size-dependent particle effective density (representing a range of potential conditions), resulting in nine IPSD estimates of PM mass corresponding to each gravimetric sample (one ULSD, one biodiesel). For the transient ULSD test, a widely used effective density distribution for fractal-like soot agglomerates resulted in good agreement between IPSD estimated mass and the gravimetric measurement (within 9% and 6% for *Soot* and *Compac*t matrices, respectively). For the steady-state biodiesel test, assuming unit density (1g/cm³ for all particles) resulted in good agreement between IPSD estimated mass and the gravimetric measurement (within 7% and 2% for *Soot* and *Compac*t matrices, respectively). These results support previous findings that the *Soot* matrix is currently the best available option for measurement of ULSD exhaust particles by the EEPS and that particle effective density distributions similar to the "fractal-like" one used here are an accurate estimate for ULSD exhaust particles under many conditions. However, based on the discrepancies between the EEPS and SMPS measured biodiesel exhaust PSDs observed here, as well as a current lack of information on the effective density of biodiesel exhaust particles, it is clear that additional research is necessary in order to understand the properties of biodiesel exhaust particles, especially as they relate to electrical mobility measurements and IPSD estimation of PM mass.

## ACKNOWLEDGMENTS

This research would not have been possible without my advisor, Dr. Britt Holmén, and the help of Tyler Feralio, John Kasumba, and Karen Sentoff.

Funding for this research came from the U.S. Department of Transportation through the University Transportation Centers Program at the University of Vermont Transportation Research Center.

***Dedicated to my parents – for everything***

## TABLE OF CONTENTS

Page

## LIST OF TABLES

**Table** Page

## LIST OF FIGURES

**Figure** Page

# CHAPTER 1: INTRODUCTION

## 1.1. Particulate Matter and Health

Particulate matter (PM) – a complex mixture of extremely small solid and liquid particles (EPA, 2009) which can be suspended in the atmosphere as an aerosol (Seinfeld & Pandis, 1998) – has important effects on human health and the environment (DeCarlo et al., 2004). The specialized cancer agency of the World Health Organization (WHO), the International Agency for Research on Cancer (IARC), has classified PM as carcinogenic to humans (IARC, 2013), with no evidence of a safe exposure level (Hamra et al., 2014). PM is associated with several health outcomes including chronic bronchitis, ischemic heart disease, stroke, respiratory infections, and exacerbation of asthma (Rushton, 2012). The health effects associated with PM are dependent on both the chemical composition of the particles as well as their physical properties (DeCarlo et al., 2004; Hinds, 1999). Because the behavior of particles (e.g., deposition efficiency in the lungs) is dependent on their size – generally, the smallest measurable particles penetrate deep into the lungs and deposit at a high rate – they are regulated and measured on a size basis (DeCarlo et al., 2004; Hinds, 1999). The US Environmental Protection Agency (EPA) currently classifies particles by two size categories: (1) "fine particles" that are 2.5μm in aerodynamic diameter ($d_a$ – defined by setting velocity) or smaller (defined as $PM_{2.5}$), and (2) "inhalable coarse particles" that are between 2.5μm and 10μm (defined as $PM_{10}$) (EPA, 2009; Hinds, 1999).

PM is generated from a variety of sources, both natural and anthropogenic (EPA, 2009). PM from diesel engine exhaust is of particular concern given that: (1) vehicle emissions are primarily responsible for fine PM in urban areas with large populations

(Robinson et al., 2010), (2) diesel engines emit greater particle mass and number than comparable gasoline engines (Kittelson, 1998), and (3) it is more difficult to control PM emissions as a result of diffusion flame combustion in compression ignition diesel engines, which results in increased soot (the elemental carbon core typical of diesel PM) formation (Heywood, 1988). Diesel PM predominately consists of elemental carbon (EC, or "soot") and organic carbon (OC – i.e., hydrocarbons) produced by incomplete combustion of fuel (Ristovski et al., 2012), and has been demonstrated to contain known carcinogens such as polycyclic aromatic hydrocarbons (PAHs) (Rushton, 2012).

## 1.2. Particulate Matter Measurement

Vehicle exhaust aerosols produced by combustion engines contain particles which continuously change after their formation, both within the exhaust system and after emission into the atmosphere (Giechaskiel et al., 2014). A number of methods have been developed in order to generate, condition, sample, and measure the properties of such aerosols. The following is a brief review of important factors pertaining to the measurement of diesel PM by gravimetric and electrical mobility methods. Much of this section is adopted from a more thorough review of vehicle particulate emissions by Giechaskiel et al. (2014).

### 1.2.1. Vehicle Exhaust Aerosols

Primary particles (10-30nm spherules) are formed during combustion by pyrolysis of the fuel (and lubricant) molecules in fuel-rich regions within the engine cylinder (Giechaskiel et al., 2014). Additionally, some fuel (and lubricant) molecules undergo incomplete combustion and are released into the exhaust stream as gaseous hydrocarbons

and sulfur compounds, which may later contribute to particle formation via nucleation or adsorption (Giechaskiel et al., 2014). The properties of these initial combustion byproducts depend on the combustion process (e.g., spark or compression ignition), fuel type/composition (e.g., gasoline or diesel), and engine operating conditions (e.g., drive cycle and engine load) (Giechaskiel et al., 2014). Primary soot particles form fractal-like agglomerates which simultaneously grow (by coagulation) and shrink (by oxidation and fragmentation) (Giechaskiel et al., 2014). The resulting number-weighted size distribution of particles formed through this process exhibits a characteristic lognormal shape, known as the diesel accumulation mode, with a mean diameter of 40-80nm (Harris & Maricq, 2002). Two additional modes (nucleation and coarse), which are formed through processes discussed later in this section, may also be present depending on a combination of factors. Whitby & Cantrell (1976) were the first do identify three distinct modes (nucleation, accumulation, and coarse – displayed as a trimodal distribution in Figure 1.1) often observed in engine exhaust aerosols.

In order to approximate the rapid changes which occur as exhaust exits the tailpipe and is abruptly diluted and cooled in ambient air, emission tests condition the exhaust gas in a dilution tunnel where it is mixed with particle-free, temperature- and humidity-controlled dilution air. Sample dilution has the additional benefits of improving measurement accuracy by removing condensation (especially that due to water) from the sample line, reducing particle concentrations to the measuring range of typical aerosol sensors, and decreasing measurement variability and uncertainty by stabilizing the particle size distribution (by slowing chemical reactions and physical transformations). The most

common dilution methods consist of either whole dilution systems with Constant Volume Sampling (CVS), which maintain a constant total sample volume by adjusting the dilution air volume, or Partial Flow Dilution (PFD) systems, which mix a constant exhaust subsample volume with a constant dilution air volume. The CVS procedure leads to a variable dilution ratio (DR, defined in Equation 1) over a transient drive cycle, but allows for simple calculation of particulate emission rates (quantity emitted per time unit – e.g., grams per second) and emission factors (emission rate per activity unit – e.g., grams per kilowatt hour) by scaling to the sample flow. PFD systems are typically smaller, less expensive, and provide a constant DR, but require measurement of the exhaust flow in order to calculate emission rates (Giechaskiel et al., 2014).

$$DR = \frac{Q_{dil,in} + Q_{exh,in}}{Q_{exh,in}} \quad [1]$$

Where:

$DR$ = dilution ratio
$Q_{dil,in}$ = dilution air inlet flow
$Q_{exh,in}$ = exhaust sample inlet flow

During dilution (full or partial), semi-volatile gases may partition into particulate matter (and vice versa) depending on the local temperature and species concentration, both of which are a function of DR (Giechaskiel et al., 2014). This partitioning from gas to solid phase occurs in the form of either adsorption onto existing soot agglomerates (i.e., “growing” accumulation mode particles) or nucleation of separate particles (i.e., the formation of liquid droplets), referred to as the diesel nucleation (alternatively known as nuclei or Aitken) mode, with maximum particle counts typically between 10-30nm

(Giechaskiel et al., 2014). The characteristics of the nucleation mode (i.e., its presence and magnitude) are difficult to predict due to its sensitivity to factors such as engine characteristics, after-treatment devices, the pre-conditioning of the engine and history of the test, fuel and lubricant properties, sampling conditions (e.g., DR, residence time, temperature) (Abdul-Khalek et al., 1998), adsorption phenomena along the sampling lines, and the amount of soot present (which promotes the competing process of adsorption) (Giechaskiel et al., 2014). A third, coarse particle mode (>2.5μm in diameter), which consists of cylinder and engine wear material as well as accumulation mode particles which are deposited on surfaces in the cylinder and exhaust system and intermittently re-entrained at a later stage, is also sometimes observed in diesel exhaust (Kittelson, 1998; EPA, 2009). Figure 1.1 (Kittelson, 1998) shows a typical diesel particle size distribution (PSD) weighted by number, mass, and alveolar (the terminal ends of the respiratory system) deposition. Note that by number, nearly all engine exhaust particles are nanoparticles – a large fraction of which are deposited in the alveoli of the lungs, which is of high concern for human health – while most of the particle mass (the current regulatory metric) exists in the accumulation mode range – which is more easily filtered by and expelled from the human respiratory system than smaller particles (Kittelson, 1998; DeCarlo et al., 2004).

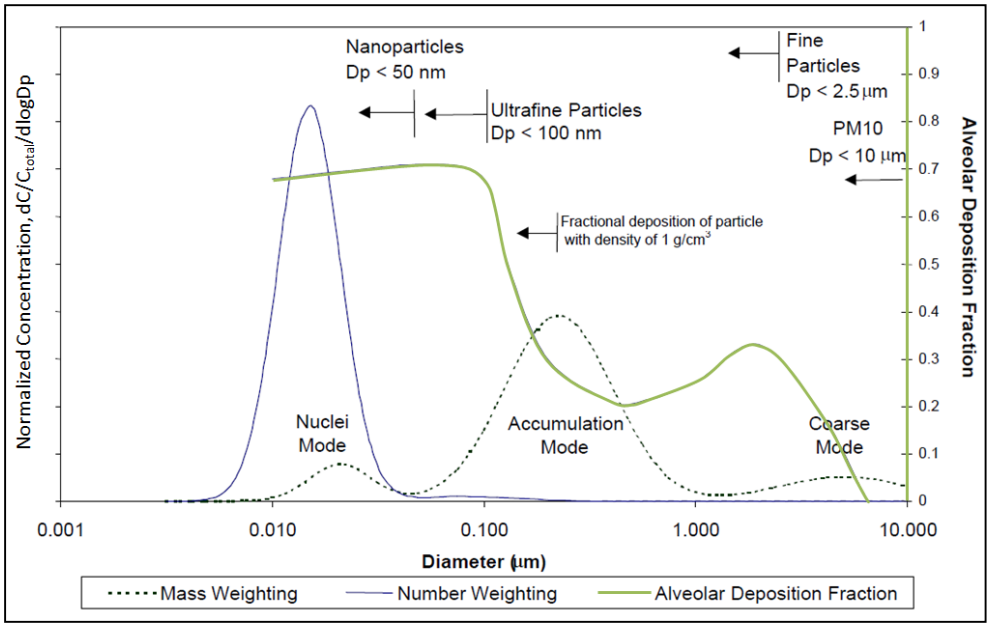


**Figure 1.1: A typical diesel particle size distribution (Kittelson, 1998)**

### 1.2.2. The Gravimetric Method

The gravimetric method provides an operational definition of PM as the mass of particles (within a certain size range) collected on a filter under specified conditions (e.g., DR and sample temperature) (Giechaskiel et al., 2014). A filter is conditioned and weighed before and after sample collection to determine the particulate mass collected, which can then be normalized to the aerosol sample gas volume (mass concentration = mass per volume; typically µg/m³) or used to calculate an emission rate (Vouitsis et al., 2003). Modern, low-emitting vehicles with current after-treatment technologies approach the detection limits of the gravimetric method, with PM collected over a standard drive cycle reaching as low as <0.1% of the blank (i.e., with no sample collected) filter mass (Giechaskiel et al., 2014). Figure 1.2 (Twigg & Phillips, 2009) shows European Union (EU) legislated PM emission limits for diesel passenger cars from 1983 to 2010, while

Figure 1.3 (adapted from Vouitsis et al., 2003) shows US and EU heavy-duty diesel engine PM emission limits from 1992 to 2010. Note that all three of the depicted standards have decreased by at least one order of magnitude over the given time period.

Figure 1.4 (Vouitsis et al., 2003) represents the increase in gravimetric measurement error associated with these increasingly stringent PM emissions limits. Several factors contribute to gravimetric measurement artifacts and uncertainty, including filter storage conditions (e.g., vapor adsorption from ambient humidity and chemical reactions influenced by sample composition and temperature), microgram balance performance, and electrostatic effects from charged particles and filter handling (Swanson et al., 2009; Giechaskiel et al., 2014). Such limitations have prompted investigation into alternative PM detection methods with greater sensitivity and resolution (i.e., real-time measurement during a drive cycle).

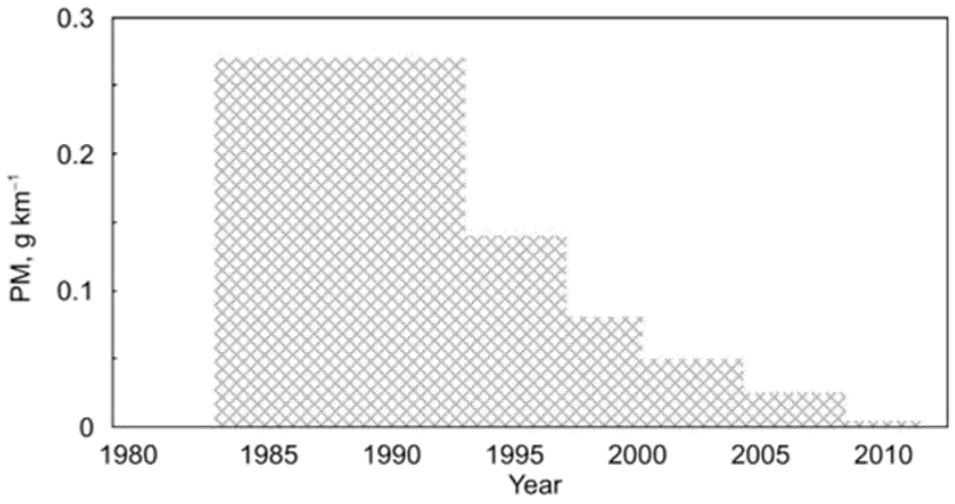


**Figure 1.2: EU legislated diesel PM emission limits for diesel passenger cars (Twigg & Phillips, 2009)**

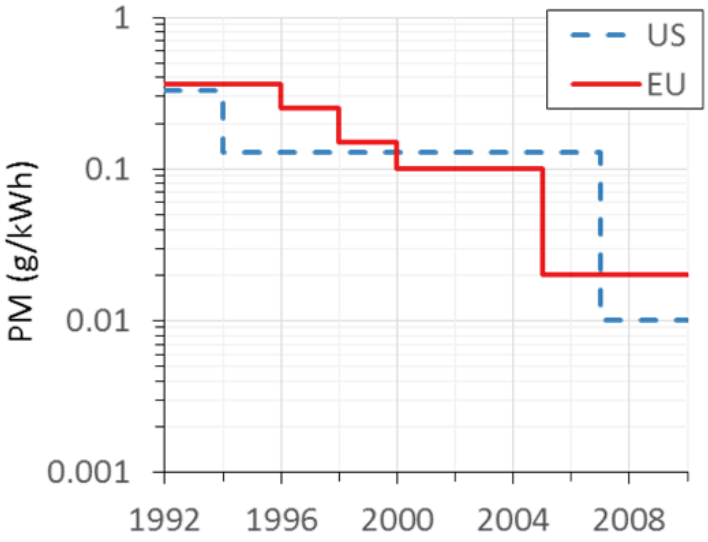


**Figure 1.3: US and EU diesel PM emission limits for heavy-duty vehicles (Vouitsis et al., 2003)**

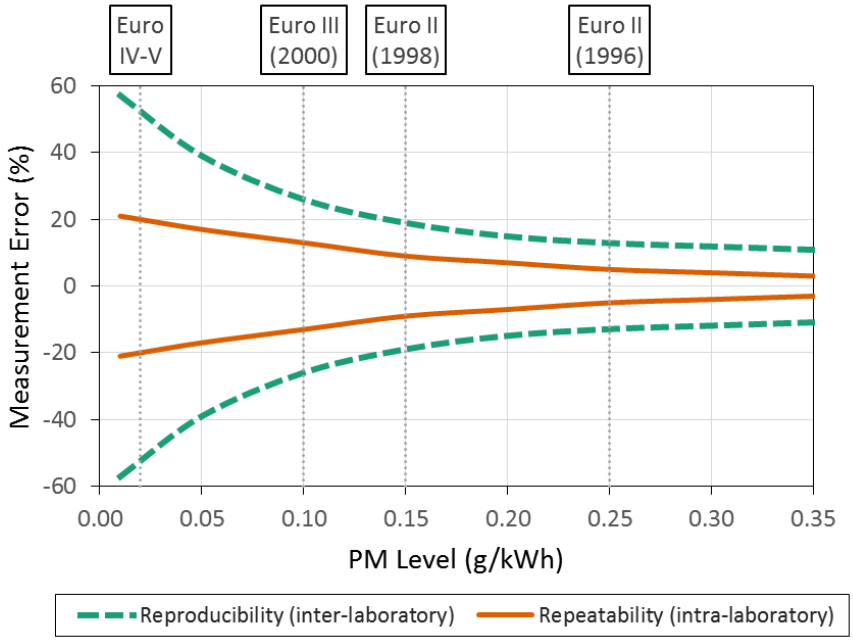


**Figure 1.4: Gravimetric measurement error associated with EU PM emission limits for heavy-duty diesel engines (Vouitsis et al., 2003)**

### 1.2.3. The Integrated Particle Size Distribution (IPSD) Method

The integrated particle size distribution (IPSD) method developed by Liu et al. (2009) estimates PM by: (1) measuring a number-weighted particle size distribution (PSD) – i.e., particles classified by their equivalent diameters (defined in Section 1.2.3.2 and depicted in Figure 1.5) and counted as particle number (PN) concentrations; (2) converting to a volume-weighted PSD by assuming spherical particles and calculating individual particle volumes from equivalent diameters in each size class; (3) converting to a mass-weighted PSD by multiplying the size-dependent values of particle volume (i.e., the volume-weighted PSD) by size-dependent particle effective density (obtained experimentally or assumed based on previous studies; typically given in $g/cm^3$ or $kg/m^3$ for each Dp, which must be converted to appropriate units to correspond with Dp units), which is dependent on particle composition and morphology; and (4) integrating the mass-weighted PSD to calculate total particle mass. An overview of the IPSD procedure is depicted in Figure 1.6. The following sections outline the general methods used to measure and/or derive PSDs, their corresponding moments (e.g., number, surface area, and volume), and particle effective density ($\rho_{eff}$).

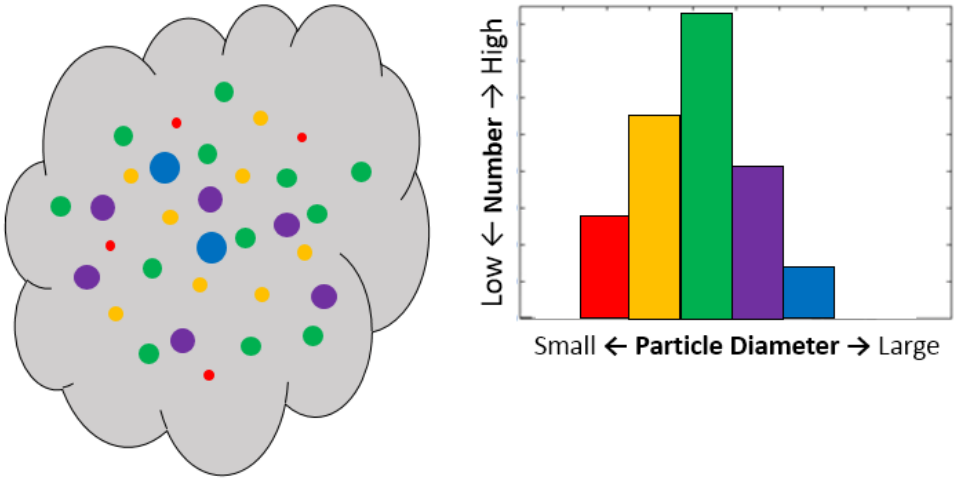


**Figure 1.5: Simplified depiction of a particle size distribution with spherical particles binned by size**

## Basic procedure

1. Measure particle size distribution (PSD) by number
2. Assume spherical particles to calculate volume
3. Apply size dependent density values to calculate mass

Method formalized by Liu et al. (2009)

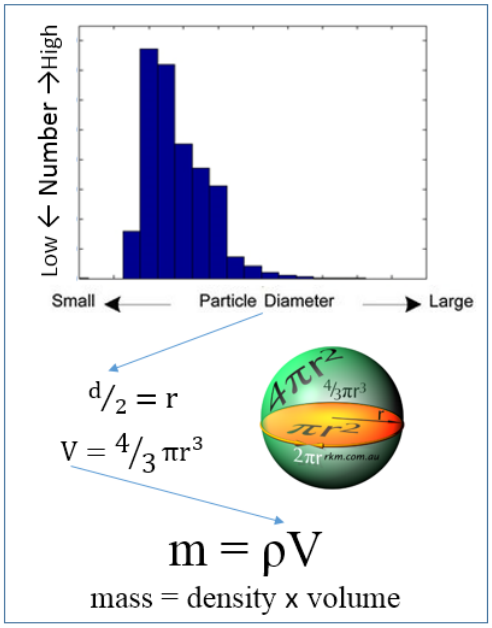


**Figure 1.6: Overview of the Integrated Particle Size Distribution (IPSD) method for estimating PM mass**

#### 1.2.3.1. Moments of the Particle Size Distribution (PSD)

A PSD is determined by the particle concentration measured in each particle size bin by an instrument – i.e. size bin defined by a particle midpoint diameter (Dp). Because the size range within each bin can vary based on the instrument's design and settings, the concentration is typically normalized to an instrument's Dp resolution (i.e., the number and range of particle diameter size bins) in order to compare PSDs across instruments. Therefore, the lognormal number concentration is typically represented as dN/dLogDp (Weber, 2012), where dN (or ΔN) is the number concentration for each particle size bin and dLogDp (or ΔLogDp) is the difference in the base 10 log of the particle diameter range of a given size bin (Hinds, 1999).

The physical property (number, length, surface area, volume, or mass) of a particle size distribution is often referred to as the $n^{th}$ (Hinds, 1999) moment of the size distribution, $Dp^n$, where the number concentration is the zeroth (n=0) moment ($Dp^0$). With a known number distribution, the other particle properties proportional to an $n^{th}$ moment of the particle diameter – length ($\sim Dp^1$), surface area, ($\sim Dp^2$), and volume ($\sim Dp^3$) – can easily be calculated with the assumption of spherical particle shape. These calculations change the weighting of each distribution so that larger size ranges (Dp) are more heavily represented with progression from the zeroth to third moments of a PSD (i.e., larger particles contribute more to mass than number). Based on the third moment (volume), a mass distribution can be calculated by multiplying by a distribution of particle densities (i.e., density values for each size bin). Therefore, both an accurate number distribution and accurate values for effective density by particle size, which is dependent on particle composition and morphology (i.e., mass concentration divided by volume concentration assuming spherical

particles), are critical to accurate calculation of a mass distribution (Weber, 2012). The total mass calculated by the IPSD method is represented by Equation 2:

$$\mathbf{M_{IPSD}} = \sum_{\mathbf{i}} \boldsymbol{\rho}_{\mathbf{i}} \times \left(\frac{\boldsymbol{\pi}}{\mathbf{6}} \times \mathbf{D}_{\mathbf{p,i}}^{\mathbf{3}}\right) \times \mathbf{n_i} \qquad [2]$$

Where spherical volumes are assumed, and:

i = index of measured particle size range (bin number)
$\rho_i$ = particle density for size bin i (generally as *effective* density)
$D_{p,i}$ = particle midpoint diameter (nm) for size bin i
$n_i$ = particle number concentration for size bin i

#### 1.2.3.2. Equivalent Particle Diameters

Because of the difficulties involved with directly measuring extremely small particles (especially in real-time and/or within a real-world environment), particles are often characterized and measured based on their size-dependent behavior under specified conditions. "Equivalent particle diameters" (Dp) are defined and interrelated by various properties of particles, such as geometric size (physical diameter: $d_p$), inertia, mobility, electrical mobility, and optical features (Giechaskiel et al., 2014). Several methods and instruments have been developed to measure the concentration of particles (typically by number or mass) as a function of their size (DeCarlo et al., 2004). Many instruments measure PSDs through a combination of size classification via electrical mobility or inertia and detection via optical properties or electrometers (Giechaskiel et al., 2014).

A particle-sizing instrument classifies particles by equivalent diameter – where the specific type of equivalent diameter depends on the instrument's operating principle (e.g., electrical mobility or inertia) – defined as the measurement yielded by the instrument for a (standard) particle with the ideal characteristics of standard density ($\rho_o$ = 1000 kg $m^{-3}$ or

1.0 g $cm^{-3}$) and spherical shape (DeCarlo et al., 2004). As particles deviate from these ideal (standard) characteristics, so does the agreement between different types of equivalent diameters. For example, an irregularly shaped particle (such as a fractal soot agglomerate) would produce different measurements of diameter via inertia (aerodynamic diameter: $d_a$) and electrical mobility ($d_m$), while the equivalent diameters measured for a standard particle would agree between these methods ($d_a = d_m$). The relationship between the aerodynamic and mobility diameters depends, in part, on the particle effective density, as discussed in Section 1.2.3.4 (DeCarlo et al., 2004; Maricq & Xu, 2004). Because this work focuses on electrical mobility measurements, Dp is used interchangeably with $d_m$ (which is a common practice in the field of aerosol science).

#### 1.2.3.3. Electrical Mobility-Based Methods

The electrical mobility diameter ($d_m$) is defined as the diameter of a sphere with the same migration velocity in a constant electric field as the particle of interest (Flagan, 2001), and depends on the shape and size of the particle (DeCarlo et al., 2004). Scanning Mobility Particle Sizer (SMPS, TSI Inc., Shoreview, MN, USA) systems, which measure $d_m$, have been widely used as the standard method to measure aerosol PSDs via electrical mobility due to their accuracy and high resolution particle sizing (Giechaskiel et al., 2014). These systems consist of two major components: (1) a Differential Mobility Analyzer (DMA) which first electrically charges particles via bipolar diffusion charging (e.g., a radioactive neutralizer) before passing them through an electrostatic classifier which only allows particles of a narrow electrical mobility range to pass through to (2) a Condensation Particle Counter (CPC), which uses laser light scattering to count particles after they are grown to

micron size in a supersaturated vapor (Giechaskiel et al., 2014). The voltage applied to the DMA can be exponentially ramped to scan over a range of particle diameters within a few minutes (Giechaskiel et al., 2014). The size classification mechanism of an SMPS is depicted in Figure 1.7 (Guha et al., 2012).

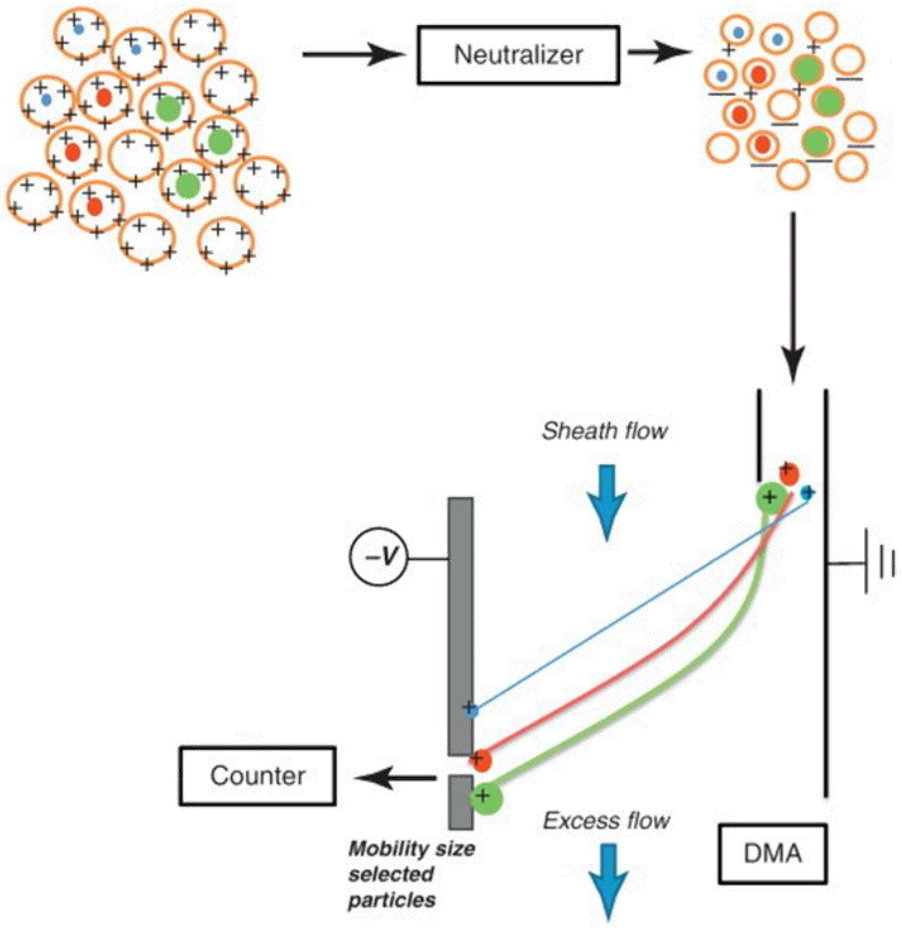


**Figure 1.7: Size classification mechanism of an SMPS (Guha et al., 2012)**

Differential mobility spectrometers (DMS) such as the Engine Exhaust Particle Sizer (EEPS) or Fast Mobility Particle Sizer (FMPS) (TSI Inc., Shoreview, MN, USA) are able to measure PSDs in real-time at 10Hz resolution, making them ideal for characterizing

engine/vehicle exhaust particles during transient drive cycles. These TSI systems (depicted in Figure 1.8) consist of a corona-wire diffusion charger, which establishes a unipolar particle charge distribution, and an electrostatic classifier with a series of rings connected to electrometers. The current produced by particle deposition onto each ring is translated into a particle number (PN) concentration for the $d_m$ size range of that ring. The corona chargers used in these systems compensate for the poorer detection sensitivity of electrometers compared to CPCs, but also produce a significant fraction of multiply charged particles which are detected at smaller diameters (Giechaskiel et al., 2014). EEPS and FMPS systems (TSI Inc., Shoreview, MN, USA) utilize a transfer function matrix – referred to as an instrument matrix (IM) by TSI – in order to compensate for time delays and multiply charged particles and translate measured electrometer currents into number-weighted PSDs (TSI, 2015). However, recent studies have revealed that the *Default* matrix (IM-2004) does not adequately compensate for the overcharging of certain particle types (Kaminski et al., 2013; Price et al., 2014; Quiros et al., 2015a; Zimmerman et al, 2014). The discrepancies between EEPS and SMPS measurements of PSDs which have been reported and attributed to their different charging mechanisms is discussed in Section 1.2.3.5.

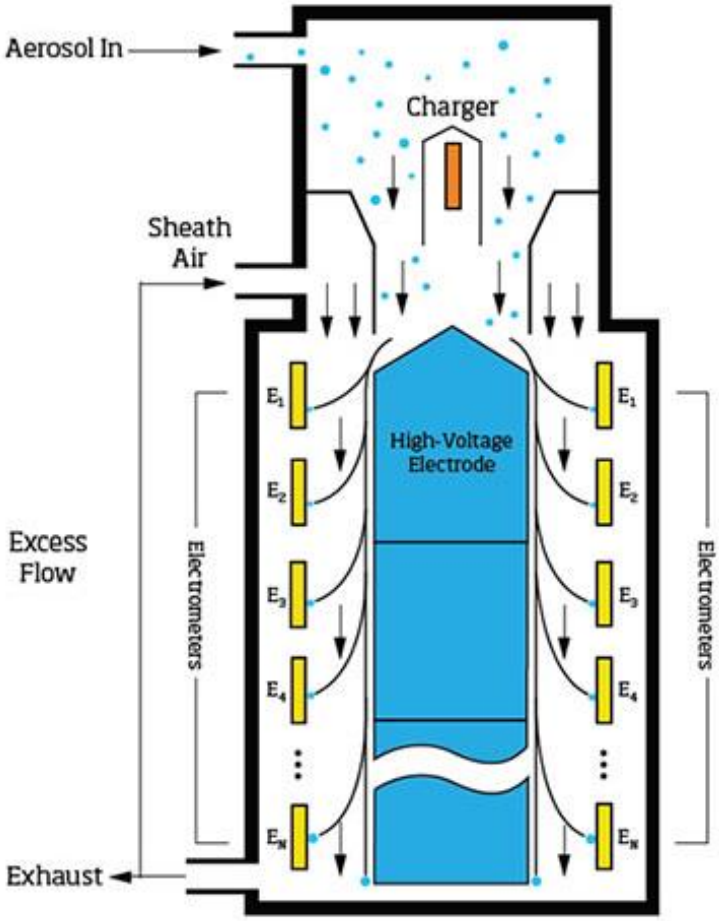


**Figure 1.8: Schematic of an EEPS and its particle sizing and counting principle (TSI, 2015)**

### 1.2.3.4. Particle Mass-mobility Scaling Exponent and Effective Density

Assuming a primary particle spherule of constant density, the mass-mobility scaling exponent (Δ) expresses the change in particle mass ($m_p$) with respect to mobility diameter – denoted as equivalent diameter (Dp, in units nm) in Equation 3 below – according to nanoparticle aggregate theory (Quiros et al., 2015a) . The mass-mobility scaling exponent is related to the arrangement of the primary particles within an agglomerate such that Δ = 1 and 3 correspond to an infinitely long straight chain-like structure and a compact sphere-like structure, respectively (Friedlander, 2000). Using a

mass constant c – called the mass-mobility prefactor, in units g/cm$^{\Delta}$ – particle mass ($m_p$) can be expressed as:

$$\mathbf{m_p = cD_p^{\Delta}} \qquad [3]$$

Particle effective density ($\rho_{eff}$, in units g/cm$^3$) is defined as the mass of a particle ($m_p$) divided by its electrical mobility equivalent volume:

$$\boldsymbol{\rho_{eff} = \frac{m_p}{\pi/_6 D_p^3}} \qquad [4]$$

Effective density is an important characteristic of particles because it determines particle transport properties and defines the relationship between mobility and aerodynamic size, as shown in Equation 5 (Kasper, 1982), where C is an appropriate Cunningham slip correction factor:

$$\boldsymbol{\rho_{eff} d_m^2 C_m = \frac{6m_p}{\pi d_m} C_m = \rho_o d_a^2 C_a} \qquad [5]$$

Combining Equations 3 and 4, effective density can be expressed as a function of a mass-mobility scaling exponent (Δ) and constant c (Xue et al., 2015):

$$\boldsymbol{\rho_{eff} = \frac{c D_p^{\Delta-3}}{\pi/_6}} \qquad [6]$$

While numerous methods exist to measure particle density, the effective density ($\rho_{eff}$) of gasoline and diesel exhaust particles has previously been characterized in several

studies by comparing mobility and aerodynamic diameter measurements (Park et al., 2003; Maricq & Xu, 2004). Several studies have reported empirical and fitted values for particle effective density for emissions from gasoline, natural gas, and diesel engines (Park et al., 2003; Maricq & Xu, 2004; Quiros et al., 2015a). The majority of studies on gasoline and diesel engines show that particle effective density decreases according to a power law as a function of particle size (Park et al., 2003; Maricq & Xu, 2004; Quiros et al., 2015a). This agrees with the power fit model for fractal aerosols because vehicle exhaust particles generally form less dense, more fractal-like agglomerates as they increase in size (i.e., accumulation mode particles). Using values of $\Delta = 2.2$ and $c = 13.3$, Xue et al. (2015) reported that the power decay model expressed in Equation 6 corresponded well to empirical results for gasoline and diesel exhaust particles generated under a range of conditions (Park et al., 2003; Maricq & Xu, 2004), but did not predict effective density well for nucleation mode particles. To overcome this issue with nucleation mode particles, Li et al. (2014) and Xue et al. (2015) assumed a constant effective density of hydrated sulfuric acid (1.46g/cm$^3$) for particles smaller than 30nm (Zheng et al, 2011). For particles between 30 and 55nm, Xue et al. (2015) assumed effective density values calculated for particles with $D_p = 55$nm (1.031g/cm$^3$), which fit well to experimental data from previous studies (Maricq & Xu, 2004; Quiros et al., 2015a). A plot of the effective density values utilized by Xue et al. (2015) is shown in Figure 1.9. This piecewise function for effective density by particle size reflects the known differences between the nucleation and accumulation modes in particle composition and formation, which may be more or less prominent depending on the test conditions.

Some studies have reported near constant effective density values for diesel PM (Quiros et al., 2015a; Symonds et al., 2007), which is likely due to the condensation of semi-volatile materials (e.g., water, sulfates, hydrocarbons) onto the solid core of fractal agglomerate spherules during dilution and cooling of the aerosol sample. Although the fractal dimension of particles can be used to characterize the change of mass with size, methods utilizing the mass-mobility scaling exponent or aerodynamic diameter account for the adsorption of semi-volatile materials onto primary spherules and, therefore, better characterize total particle mass (and density) as a function of size (Quiros et al., 2015a). Quiros et al. (2015a) reported a range of mass-mobility scaling exponents for various engine operating conditions. An alternative estimate of effective density (using values of $\Delta = 2.96$ and $c = 0.9$ based on Quiros et al., 2015a) for cases where the measured PM may have a large amount of adsorbed materials (which may be the case for biodiesel emissions under certain conditions, as discussed in Section 1.3) is also shown in Figure 1.9, along with standard (unit) particle density for reference.

The two empirical effective density distributions in Figure 1.9 demonstrate the wide range of effective density values which have been measured for soot particles (which is also demonstrated well in Quiros 2015a). Unit density is roughly in the middle of these two extremes for accumulation mode particles, where the majority of soot PM mass exists (Kittelson, 1998). The effective density function from Maricq & Xu (2004) – similar to that for Xue et al. (2015) – and unit density have been widely used to estimate the effective density of soot particles (Li et al., 2014). However, to utilize only one of these effective density distributions in an application such as the IPSD method without sufficient empirical

evidence that they are representative of the particles being studied may be inappropriate considering the wide range of possible effective density values and the potential sensitivity of calculated PM mass to these values (Li et al., 2014). Although it may be impractical to determine specific empirical values of size-dependent effective density for each application of the IPSD method (e.g., in each unique emissions test), it may be advisable to at least calculate a range of IPSD estimated PM mass values utilizing sets of effective density distributions which represent the anticipated range of effective density values that may be encountered (such as those shown in Figure 1.9).

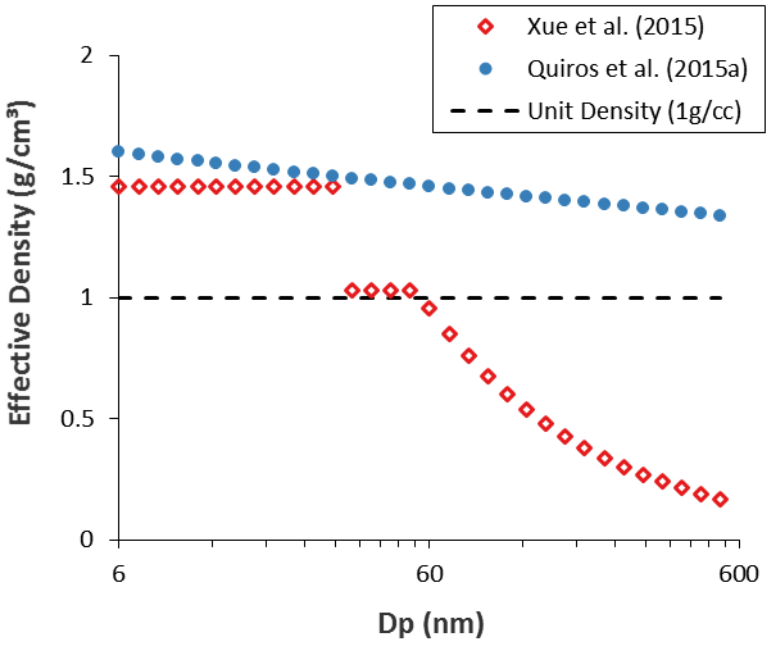


**Figure 1.9: Soot particle effective density values (Xue et al., 2015; Quiros et al., 2015a) and unit density**

#### 1.2.3.5. EEPS vs. SMPS

Large differences (typically ±30%, but up to a factor of 3) have been reported between the results from EEPS/FMPS systems compared to SMPS-derived PSDs (Kaminski et al., 2013; Price et al., 2014; Quiros et al., 2015b; Zimmerman et al, 2014). Zimmerman et al. (2014) found that the agglomerate nature of diesel soot was associated with substantial overestimates in PN concentrations in the 20-120nm size range, while Kaminski et al. (2013) found both over- and under-estimations associated with diesel soot agglomerates. Wang et al. (2016a & 2016b) explain that unipolar charging of particles depends on particle morphology – a more fractal-like particle has greater surface area and therefore greater capacitance (Shin et al., 2010).

In response to these discrepancies, TSI developed two new instrument matrices, referred to here as "calibration matrices", which translate electrometer currents into particle counts (utilizing assumed constants and the transfer function) at certain Dp size ranges (bins) (TSI, 2015). The "*Soot*" matrix was developed for engine exhaust (i.e., fractal-like) particles (Wang et al., 2016b), while the "*Compact*" matrix was developed for improved measurement of compact shape particles compared to the original "*Default*" matrix (Wang et al., 2016a). Wang et al. (2016b) reported that geometric mean diameters (GMDs) measured with the *Soot* matrix agreed within ±20% to those measured by an SMPS for 9.5-400nm monodisperse diesel engine exhaust particles.

##### 1.2.3.5.1. Prior Evaluation of EEPS *Soot* Matrix for Engines/Vehicles

Xue et al. (2015) evaluated the recently released EEPS *Soot* matrix relative to an SMPS for particles of various morphologies generated from five different combustion sources under steady-state conditions: (1) a diesel generator operating on ultra-low sulfur

diesel (ULSD), (2) a diesel generator operating on 100% soybean biodiesel, (3) a gasoline direct-injection (GDI) vehicle, (4) a conventional port-fuel injection (PFI) gasoline vehicle, and (5) a light-duty diesel (LDD) vehicle equipped with a diesel particulate filter (DPF). They found that the new *Soot* matrix generally resulted in better agreement with the SMPS, except when challenged by a distinct nucleation mode during high-load operation of the LDD vehicle (Xue et al., 2015).

## 1.3. Biodiesel PM Emissions

The term "biodiesel" commonly refers to a mixture of fatty acid methyl esters (FAMEs) consisting of long-chain alkyl esters which contain two oxygen atoms per molecule (Giakoumis et al., 2012; Lapuerta et al., 2008). Biodiesel is produced from the transesterification of lipids (typically vegetable oils or animal fats) with an alcohol (typically methanol) in the presence of a catalyst (i.e., sodium or potassium hydroxide) (Xue, 2013). Popular lipid feedstocks for biodiesel production include soybean, rapeseed (canola), and waste cooking oils (Giakoumis et al., 2012). Multiple advantages have been associated with the use of biodiesel over conventional petroleum-based diesel (petrodiesel), including decreased emissions of several pollutants, such as PM (EPA, 2002; Giakoumis et al., 2012; Lapuerta et al., 2008). In general, these changes in emissions have displayed a nearly linear trend as biodiesel is used in greater blend proportions with petrodiesel (see Figure 1.10); from B0 indicating neat petrodiesel to B100 which indicates neat biodiesel.

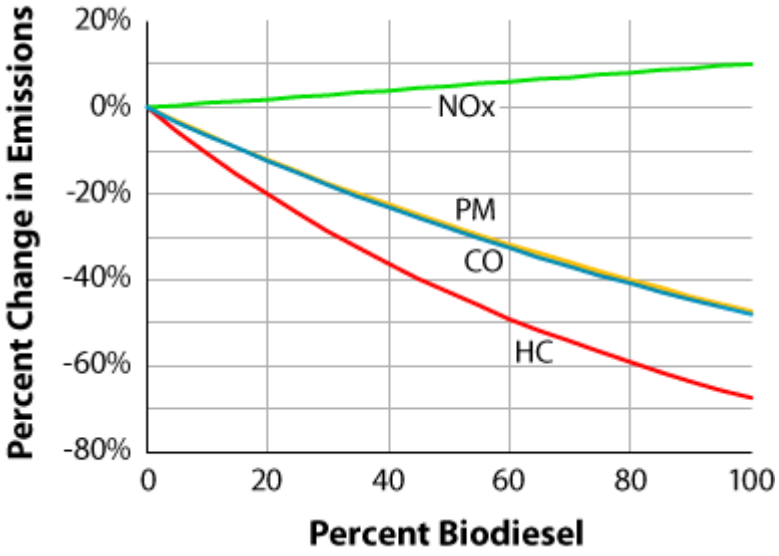


**Figure 1.10: Average emission impacts of biodiesel for heavy-duty highway engines (EPA, 2002)**

Lower PM emissions with biodiesel use have been attributed to conditions associated with complete combustion and/or soot oxidation (Lapuerta et al., 2008). Key factors which promote these conditions include the oxygen content of FAMEs, the absence of sulfur in biodiesel (considered a soot precursor), and advanced start of injection/combustion (promoting soot oxidation) (Lapuerta et al., 2008). Other reasons to explain reductions of PM emissions with the use of biodiesel include the absence of aromatic compounds (considered soot precursors), the formation of lower density soot particles (providing more soot surface area available for oxidation), and the lower final boiling point (the maximum temperature observed during distillation) of biodiesel compared to petrodiesel (i.e., less soot formation from heavy hydrocarbons which do not vaporize) (Lapuerta et al., 2008).

While the majority of biodiesel studies have demonstrated a decreasing trend in PM emissions with the use of biodiesel, some studies have demonstrated a substantial increase

in biodiesel PM mass and, especially the soluble organic fraction (SOF), which may be a result of the test drive cycle (i.e., a transient drive cycle with relatively cold combustion/exhaust temps which promotes SOF formation and adsorption) or the fuel injection strategy of the engine used in the study (e.g., a greater mass of biodiesel fuel may be injected into the combustion chamber relative to diesel), or some combination of drive-cycle, fuel injection strategy, fuel properties, and temperature (ambient and combustion) (Giakoumis, 2012).

Fontaras et al. (2009) tested soybean-based biodiesel (B0, B50, B100) in a Euro 2 passenger car (VW Golf 1.9L TDi) on the New European Driving Cycle (NEDC) and observed a 177% increase in PM emissions with B100 compared to B0 over the entire cycle, with a 278% increase in PM emissions during the urban driving cycle (UDC) portion of the cycle, which consists of a cold engine start. Martini et al. (2007) also observed an increase in PM emissions over the UDC when using neat biodiesels (rapeseed and a blend of sunflower and soybean) on a Euro 3 light-duty vehicle. Bielaczyc et al. (2009) tested rapeseed biodiesel (B0, B30, B50, B100) in a Euro 4 passenger car (1.4L, common rail direct injection) and observed a 338% increase in PM emissions over the NEDC, with a 890% increase during the UDC phase. Yehliu et al. (2010) demonstrated an increase in both PM mass and number with B100 soybean biodiesel, as well as a much more substantial decrease in particle concentrations in a number-weighted PSD (via SMPS) with the use of a thermodenuder for biodiesel than ULSD, demonstrating that the biodiesel particles contained a large fraction of condensed organics (i.e., OC). Surawski et al. (2011) estimated a similar increase in SOF with soy, tallow, and canola biodiesel relative to

ULSD. They also suggested a concomitant decrease in the surface area of the core particles (EC remaining after heating with thermodenuder) for all biodiesel blends, however this estimate relied on the assumption of spherical particles which is not appropriate for agglomerates. Comparing 100% biodiesel to ULSD, Zhang et al. (2011) observed a decrease in PM emissions under high engine load and an increase at low load, attributing the decrease at high load to improved oxidation of locally fuel-rich combustion areas (Tsolakis et al., 2007), and the increase at low load to the higher viscosity of biodiesel compared to ULSD, resulting in worse vaporization and atomization at lower temperature (Wu et al., 2009).

Considering the observed effects of biodiesel on gravimetrically measured PM with certain conditions, it is possible that biodiesel may result in unique exhaust particle properties (e.g., morphology, density, chemical composition), which may in turn affect unipolar charging and therefore accurate measurement by electrical mobility instruments such as the EEPS. Considering morphology, biodiesel may produce smaller primary particles (Smekens et al., 2005; Merchan-Merchan et al., 2012; Hwang et al., 2015) or larger (Ye, 2015) primary particles than ULSD – potentially via a different soot inception pathway and/or greater oxidation of primary soot particles. Smaller primary particles may result in agglomerates with greater surface area and capacitance, resulting in overcharging of such agglomerates (Shin et al., 2010). Additionally, greater polydispersity in primary particle size (i.e., both smaller and larger primary particles) could also affect agglomerate surface area and subsequent unipolar charging (Dastanpour & Rogak, 2016).

Although the material composition of particles is not believed to affect unipolar charging (Shin et al., 2009; Kulkarni et al., 2011), this has not been thoroughly investigated for polar compounds such as biodiesel. Biodiesel particles generally consist of a relatively larger fraction of organic carbon (OC), or basically a higher soluble organic fraction (SOF), than diesel particles (Chung et al., 2008). Adsorbed SOF, which may consist of unburned biodiesel, on agglomerate biodiesel particles may affect unipolar charging not only due to chemical composition, but could also result in unique particle morphology. Additionally, a soot particle coated with OC may be more hygroscopic than high EC soot particles (Vu et al., 2015), promoting water condensation onto the particle and influencing morphology, density, and unipolar charging.

### 1.4. Objectives of this Thesis

This work extends upon that of Xue et al. (2015) which evaluated the EEPS *Soot* matrix (relative to *Default*) for ULSD and biodiesel emissions from a generator under steady-state conditions with the SMPS as the gold standard reference. Here, it is not assumed that the *Soot* matrix will provide the best results and all three available calibration matrices for the EEPS (*Default*, *Soot*, and *Compact*) are evaluated against an SMPS for ULSD and biodiesel emissions generated from a light-duty diesel engine operating under steady-state conditions at 75% engine load. Additionally, gravimetric measurements (one from a transient ULSD test, one from the steady-state biodiesel test) are used as references to determine how well PSD data produced from each EEPS matrix estimate PM mass when used in the IPSD method (with reasonable assumptions for effective density). It is anticipated that the results from this work will either help to support the assumption that

the new *Soot* matrix is appropriate for universal application to measurement of engine/vehicle exhaust particles, or demonstrate that additional matrices (either provided by TSI or custom-made by users) are necessary.

# CHAPTER 2: METHODOLOGY

## 2.1. Engine Specifications

The light-duty diesel engine used in this study was a naturally aspirated, four cylinder Volkswagen 1.9L SDi engine with a pump-line-nozzle fuel injection system coupled to an Industrias Zelu, S.L. K-40 power absorber unit (eddy current dynamometer) (Table 2.1). The engine conforms to emission certification EC 97/68 Stage IIIA and is similar to those in EURO II Volkswagen LDD automobiles. The engine was not equipped with an exhaust gas recirculation system or any exhaust after-treatment devices – the emissions data reported are engine-out.

**Table 2.1: Engine and dynamometer specifications**

| **Engine** | |
|---|---|
| Manufacturer: | Volkswagen |
| Identification Code: | ARD |
| Charge Air: | Naturally Aspirated |
| Capacity: | 1896cm$^3$ |
| Cylinders: | 4 |
| Bore: | 79.5mm |
| Stroke: | 95.5mm |
| Compression Ratio: | 19.5:1 |
| Nominal Output: | 44 kW @ 3600 RPM |
| Max Torque: | 130Nm @ 2000 - 2400 RPM |
| Minimum CN: | 49 |
| Control System: | Bosch EDC |
| Fuel Injection: | Bosch VE injection pump |
| EGR: | None |
| **Power Absorption Unit/ Eddy Current Dynamometer** | |
| Manufacturer: | Zelu/ Klam |
| Model Number: | K-40 PAU |
| Max Power: | 60kW |
| Max Torque: | 145Nm |

## 2.2. Fuel Specifications

The fuels used for this study were ultra-low sulfur diesel (ULSD) acquired from Trono Fuels (Burlington, VT) and commercial neat soybean-oil-based biodiesel from Dennis K. Burke Inc. (Chelsea, MA). Fuel densities, determined with a densitometer equipped in a mid-FTIR analyzer (IROX-D, Grabner Instruments, Vienna, Austria), were 0.81g/cm³ for ULSD and 0.86g/cm³ for biodiesel. Gas chromatography-mass spectrometry (GC-MS) analysis of the n-alkane profile of the ULSD was performed (Figure 2.1), as well as the fatty acid methyl ester (FAME) profile of the biodiesel fuel (Figure 2.2) (Kasumba, 2015). The ULSD fuel used in this study primarily consisted of aliphatic hydrocarbons with 10-25 carbon atoms, which is typical of diesel fuel and comparable to the results from Schauer et al. (1999). The two major FAMEs found in the soybean-oil-based biodiesel were linoleic and oleic acid methyl ester, which is consistent with the results from Hoekman et al. (2012).

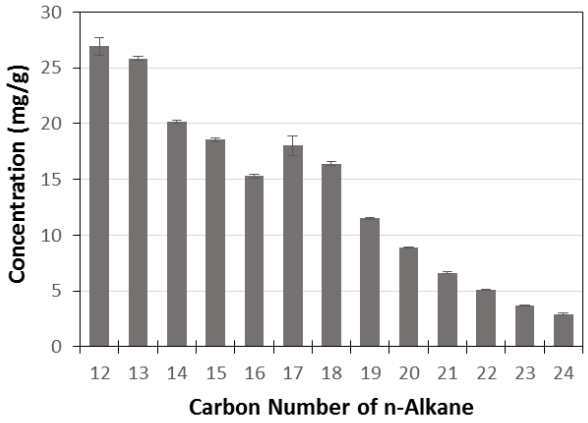


**Figure 2.1: Concentration of n-alkanes in ULSD as determined by Kasumba (2015)**

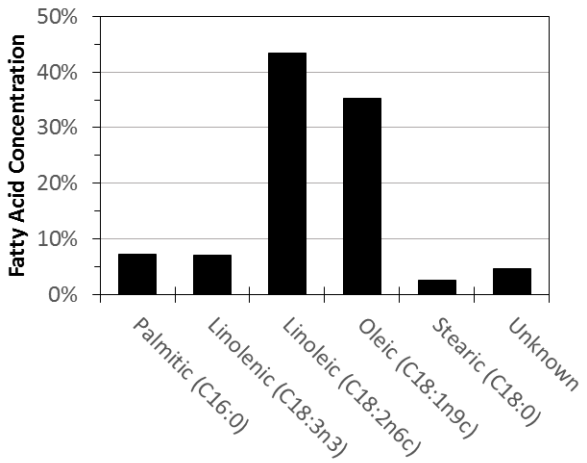


**Figure 2.2: Percent composition of FAMEs in soybean biodiesel as determined by Kasumba (2015)**

## 2.3. Engine Operation

### 2.3.1. Steady State

Following ignition, the engine was allowed to idle for 7.5 minutes, followed by a 7.5 minute warm-up sequence conducted at 3300rpm and 45% throttle. Data and filter samples were collected after the engine reached steady-state conditions of 2200rpm and 67% throttle (~75% engine load). Steady-state emissions samples were collected for ≥90 minutes before the engine was again brought to idle where it was allowed to cool-down for 7.5 minutes before being turned off.

### 2.3.2. Transient

To simulate real-world urban driving, a transient drive cycle was developed by PhD student Tyler Feralio with OBD-II engine speed and throttle position data collected from a 2003 Volkswagen TDi Jetta sedan (ALH engine code) with an automatic transmission as it drove a predefined route through downtown Burlington, VT (Holmén et al., 2014). The TDi engine in this on-road vehicle is essentially a turbocharged version of the SDi test engine.

The developed drive cycle contained a 60-minute transient portion (developed with the on-road VW Jetta data; average engine load of 12%) and three 10-minute steady-state portions (defined by RPM) with average nominal percent loads of 35, 10, and 75% (calculated with the torque curve supplied by Volkswagen) respectively. The transient phase commenced after warming the engine up by running it at 3000RPM and 60% throttle until the coolant temperature stabilized at 92±2°C.

## 2.4. Operational and Emissions Data Collection

### 2.4.1. Exhaust Dilution

A modified Dekati (Kangasala, Finland) ejector diluter was designed to provide a target constant dilution ratio (DR) of 80. Dilution air and exhaust sample temperatures were maintained at 30°C and 110°C, respectively, as they entered the ejector diluter. Second-by-second diluter inlet flow rates were measured with custom inline orifice flow meters which consisted of Dwyer 605 transmitting Magnehelics® measuring the pressure difference across inline orifices (see Figure 2.3). Given that the temperature and pressure of the dilution air and exhaust sample inlet gases were controlled, the recorded data are measures of mass flow rate. Real-time DR was determined based on 1Hz LabView (ver. 8.6.1) recordings of flow rates. Reported EEPS data (also 1Hz) were normalized to corresponding second-by-second DR, while SMPS data were normalized to average values of DR from the time period corresponding to each 135 second sample. Average dilution ratios (± one standard deviation) of 74.8 ± 3.1 and 85.8 ± 1.2 were achieved for each test, ULSD and biodiesel, respectively. More detail regarding the dilution system can be found in Holmén et al. (2014).

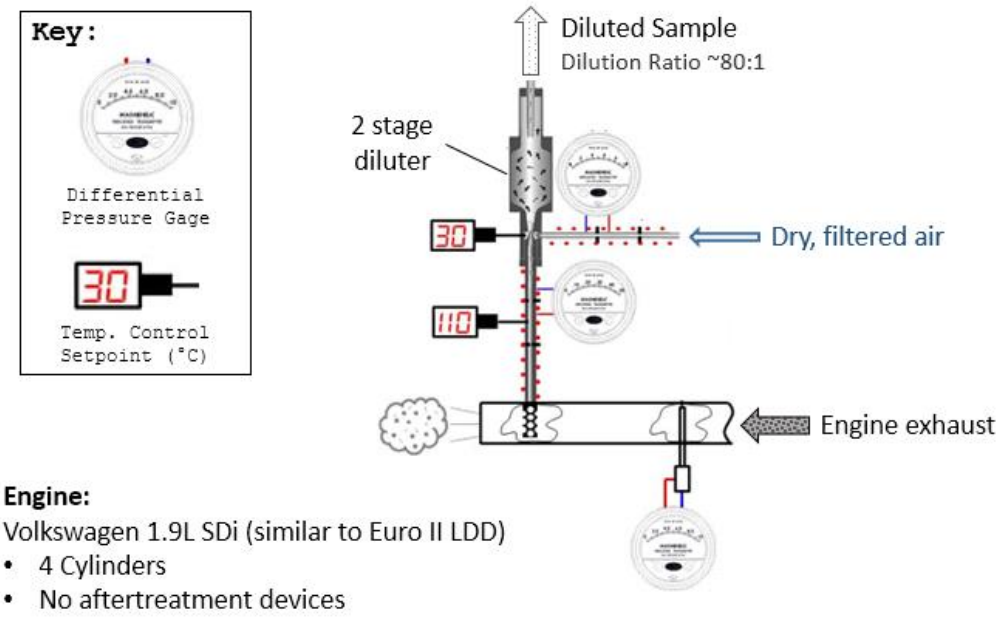


**Figure 2.3: Engine exhaust dilution system (diagram by Tyler Feralio; Holmén et al., 2014)**

### 2.4.2. Instrumentation

Engine operating conditions, dilution conditions, and EEPS PSDs were measured and recorded simultaneously at a sampling rate of ≥1Hz. Engine conditions were recorded via a Ross-Tech VCDS scan tool (ver. 11.11.6) from the engine control unit (ECU) and the engine/dynamometer control software, Armfield ArmSoft (ver. 1.43), from auxiliary sensors. Additional engine and dilution system conditions were logged with a National Instruments data acquisition system (LabView, ver. 8.6.1). EEPS and SMPS data were time aligned with the engine operational data to take into account the time needed for the exhaust sample to travel from the sample port in the exhaust system to each instrument.

Number-weighted PSD (#/cm$^3$) data were collected at 1Hz with a TSI Inc. (Shoreview, MN, USA) 3090 Engine Exhaust Particle Sizer (EEPS; 16 channels per decade, 32 channels from 5.6-560nm). The bounds and midpoint for each EEPS size bin

can be found in Table A.2 in the Appendix. The EEPS operates at 10 L/min for sample air and 40L/min for sheath air, with an inlet cyclone aerodynamic cut-off diameter ($d_{50}$) of 1μm. The TSI SMPS (Model 3936), consisting of a Differential Mobility Analyzer (DMA, Model 3081) and a butanol-based Ultrafine Condensation Particle Counter (CPC, Model 3025A), was operated with an impactor featuring a 0.071cm diameter nozzle orifice (aerodynamic cut-off diameter of 592nm). For each steady-state test (ULSD and biodiesel), the SMPS was configured with aerosol and sheath flows equal to 1.5 and 15 L/min, respectively, a sample scan duration of 135 seconds (single scan, up scan 120 seconds, retrace time 15 seconds), and therefore measured number-weighted PSDs from 5.8-229nm over 102 size bins (64 channels per decade). The bounds and midpoint for each SMPS size bin can be found in Table A.3 in the Appendix.

Samples for gravimetric analysis were collected for the duration of each test cycle (90 minutes of steady state for biodiesel, 60 minutes of transient + three 10 minute steady-state phases for ULSD). Exhaust particles were sampled on Teflon-coated Fiberfilm filters (FF, T60A20, diameter 47 mm, Pallflex Corp., Putman, CT). Exhaust flowed through each filter at 11.4 ± 0.4 L/min for the biodiesel PM sample and 18.1 ± .02 L/min for the ULSD PM sample. Flow-rates were measured before and after each test and were used, along with the time sampled, to estimate the total volume sampled. All filters were pre-weighed and post-weighed (after conditioning for 24 hours in a Coy chamber maintained at 20-25 °C and 30-40% relative humidity) in order to determine the gravimetric mass of the sampled exhaust PM. A Cahn microbalance (Cahn C-33, Thermo Scientific, Waltham, MA) with

1μg sensitivity was used for weighing the filters. Mass concentrations were determined by dividing the mass collected on each filter by the estimated total volume sampled.

### 2.5. Quality Assurance

Before and after each test, quality assurance (QA) data were collected. Two types of "blank" samples were collected: (1) an "instrument blank" in which the instrument sampled HEPA filtered room air, and (2) a "tunnel blank" in which the instrument sampled air from the active dilution system while the engine was not running. The sampling sequence for each test is detailed in Table 2.2 and QA data results are summarized in Appendix A.1. The minimum total particle number (TPN) concentration measured by the SMPS during both emissions tests (ULSD and biodiesel) was $9.8 \times 10^3$, while the maximum SMPS blank (instrument and tunnel) TPN concentration measured was $393/cm^3$ (<5% of emissions tests max), demonstrating a very low measurement error associated with the SMPS instrument itself and the sampling conditions (tunnel blank).

The minimum TPN concentration measured by the EEPS (*Default* matrix) during both emissions tests was $1.4 \times 10^4$, while the maximum EEPS blank (*Default* matrix) TPN concentration was $8.7 \times 10^3$, (~61% of emissions tests max). This high degree of error associated with the EEPS relative to the SMPS is largely due to the EEPS mechanism of operation and the noise associated with the electrometers that the instrument uses to measure particles (TSI, 2006). This is demonstrated by the observation that the maximum EEPS instrument blank (*Default* matrix) TPN concentration was $5.7 \times 10^3$, (~41% of emissions tests max). Individual EEPS electrometers were determined to be operating within prescribed parameters (TSI, 2006) by: (1) checking electrometer drift (current

offsets before and after emissions tests) against ideal values listed in the manual, and (2) verifying that the particle number concentration measured for each particle size bin during pre-test instrument blanks was below the minimum detection limit of the instrument (see Appendix, Figure A.2). Despite the greater amount of noise associated with EEPS measurements, the QA results for both instruments indicate that they were both working according manufacturer specifications.

**Table 2.2: The data collection sequence for each test**

| Event | Setting | Duration |
|---|---|---|
| ***Instrument Blank (preIB)*** | ***Instrument on HEPA filter*** | ***≥10min*** |
| **Tunnel Blank (preTB)** | **Dilution System On** | **≥10min** |
| **Engine Idle** | **Engine On** | **7.5min** |
| **Engine Warm-up** | **3300rpm, 60% Throttle** | **7.5min** |
| **Test Cycle** | **Steady State or Transient** | **~90min** |
| **Engine Cool-down (Idle)** | **Engine On** | **7.5min** |
| **Tunnel Blank (postTB)** | **Dilution System On** | **≥10min** |
| ***Instrument Blank (postIB)*** | ***Instrument on HEPA filter*** | ***≥10min*** |

### 2.6. Data Selection

In order to analyze and compare stable PSDs, SMPS data were selected based on preliminary analyses of 1Hz data for calculated dilution ratio (DR) for the two steady-state tests (ULSD and biodiesel). Continuous ranges of real-time data were selected during which the all values for DR were ≤5% of the average for that time period. Due to greater variation in DR values during the ULSD test, this resulted in a total of 10 SMPS scans for

the ULSD test and 40 SMPS scans for the biodiesel test. EEPS data from the same time periods were used for comparison to average SMPS PSDs, resulting in 1350 seconds (22.5 minutes) of EEPS data for the ULSD test and 5400 seconds (90 minutes) for the biodiesel test. Because a filter sampled during the same time period in the biodiesel test, the same EEPS and SMPS data were used in the IPSD method to compare calculated PM to that measured gravimetrically. A gravimetric sample was not collected during the steady-state ULSD test, however, a gravimetric sample and EEPS data were available from a transient ULSD test. For this transient ULSD test, 5700 seconds (95 minutes) of EEPS data corresponding to the sampling time period of the filter were used in the IPSD method.

### 2.7. PSD Data Analysis

Using the latest release of the TSI EEPS software (version 3.2.5.0), the EEPS PSD data were exported for all three inversion matrices (*Default*, *Soot*, and *Compact*) from previously collected raw instrument data records with the user-selectable menu option. PSDs were fit to lognormal distributions where modes (nucleation, accumulation, and coarse) were manually determined from log-log and semi-log plots of the data. For each mode that was present, the corresponding geometric mean diameter (GMD) and geometric standard deviation (GSD) was calculated based on Equations 7 and 8, respectively (Hinds, 1999):

$$\mathbf{GMD} = (\boldsymbol{D_1^{n_1} D_2^{n_2} D_3^{n_3} \ldots D_N^{n_N}})^{1/N} \quad [7]$$

$$\mathbf{logGSD} = \left[\frac{\sum \mathbf{n_i (logD_i - logGMD)^2}}{\mathbf{N-1}}\right]^{1/2} \quad [8]$$

Where:

i = index of measured particle size range (bin number)
$D_i$ = midpoint particle size
$n_i$ = number of particles in group i having midpoint size $D_i$
$N = \Sigma n_i$ (the total number of particles, summed over all intervals)
log = common logarithm (with base 10)

## 2.8. Calculated PM ($M_{IPSD}$) Data Analysis

EEPS and SMPS PSDs were used to calculate real-time PM mass with the IPSD method as outlined in Section 1.2.3. PSDs exported from all three EEPS matrices (*Default*, *Soot*, *Compact*) were used, as well as the three effective density distributions described in Section 1.2.3.4 and shown in Figure 1.9 (3 EEPS matrices x 3 density distributions = 9 estimates of PM). For simplicity, those density distributions will be referred to as "*Unit ρ*", "*Fractal ρ*", and "*Adsorbed ρ*", as shown in Figure 2.4 (which corresponds to Figure 1.9).

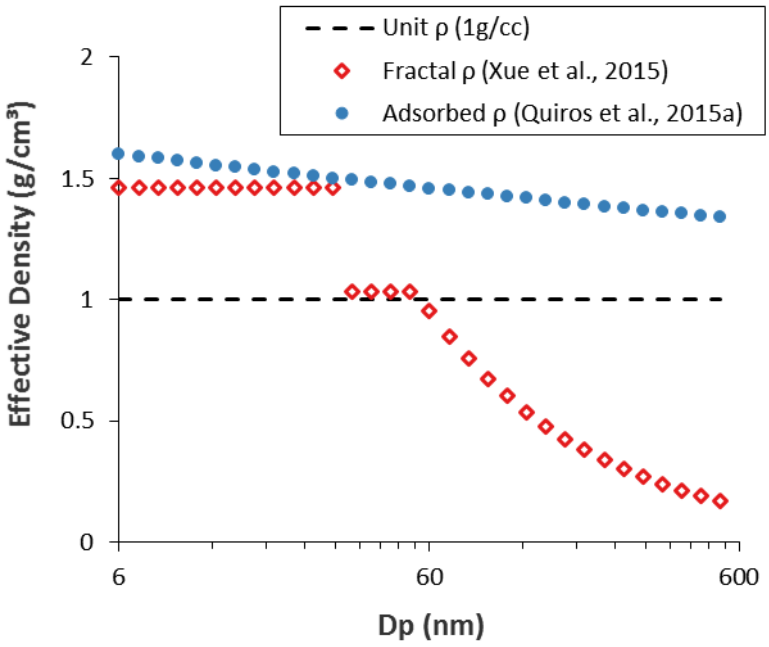


**Figure 2.4: Particle effective density values used in this study**

# CHAPTER 3: RESULTS & DISCUSSION

## 3.1. Overview of Test Conditions

Table 3.1 provides an overview of the experimental conditions recorded for each test. In general, conditions were similar between the three tests, however the differences in dilution ratio (DR), temperature, and relative humidity (RH) are worth noting. Although data are corrected for DR, and air used for dilution was treated (i.e., filtered, heated, and dried), the differences in DR, temperature, and RH may have affected the formation of nucleation mode particles which are highly sensitive to these conditions (Abdul-Khalek, 1998). This issue is not pertinent to the purpose of this thesis, which is a comparison between instruments under a limited set of conditions. However, in a more systematic study of the measurement capabilities of the EEPS compared to the SMPS, it will be important to challenge the instruments with exhaust particles generated from a wide range of conditions likely to occur in the real world (e.g., engines, fuels, drive cycles, seasons).

**Table 3.1: Overview of steady-state emissions tests conducted**

| | Fuel | ***ULSD*** *(100%)* | ***Biodiesel*** *(100% Soy Methyl-Ester)* | ***ULSD*** *(100%)* |
|---|---|---|---|---|
| | **Test ID** | 1_07MAY2012_B0 | 1_16MAY2012_B100 | 1_15MAY2013_B0 |
| | **Engine Cycle** | Steady State 75% Load | Steady State 75% Load | Transient |
| | **Dilution Ratio** | 74.8 ± 3.1 | 85.8 ± 1.2 | 83.3 ± 7.6 |
| Conditions at Beginning of Test | **Ambient Temp. (°C)** | 21.3 | 21.8 | 18.3 |
| | **Ambient Relative Humidity (%)** | 19.7 | 63 | 23.1 |
| | **Barometric Pressure (mmHg)** | 763.8 | 757.9 | 751.8 |
| | **Particle Data Collected** | EEPS, SMPS | EEPS, SMPS, Gravimetric | EEPS, Gravimetric |

## 3.2. Comparison of PSDs from Steady-State Tests (EEPS vs. SMPS)

### 3.2.1. ULSD Steady-State PSDs

Average PSDs measured by each EEPS matrix and the SMPS are shown on both a log-log plot (Figure 3.1) and semi-log plot (Figure 3.2), where vertical error bars represent one standard deviation (±σ). PSDs were fit to lognormal distributions and corresponding GMDs and GSDs are listed in Table 3.2. A log-log plot of these lognormal fits are shown in Figure 3.3. All EEPS ULSD measurements displayed a weak nucleation mode and a more distinct accumulation mode, while only an accumulation mode was observed with the SMPS. This was not due to a difference in size range, as both instruments measured a similar minimum Dp: EEPS (5.61nm), SMPS (5.83nm). However, the transfer line (i.e., sampling tube) between the dilution system and the SMPS was substantially longer than

that between the dilution system and EEPS (approximately 2m and 6m, respectively), potentially resulting in a greater loss of nucleation mode particles due to adsorption along the line (Giechaskiel et al., 2014). While the resulting EEPS data processed by all three matrices (*Default*, *Soot*, and *Compac*t) exhibited a nucleation mode with a GMD around 9-10nm and GSD between 1.31 and 1.43, the SMPS detected no particles ≤14.6nm. This appears contrary to the result from Xue et al. (2015), where measurements from a LDD vehicle showed a distinct nucleation mode via SMPS measurements and a weak nucleation mode via EEPS *Default* and *Soot* matrix measurements. However, their results for a diesel generator exhibited a similar pattern as presented here for nucleation mode particles – where the mode was detected by the EEPS but not by the SMPS. As noted previously in Section 1.2.1, the presence and magnitude of the nucleation mode is often highly variable due to its sensitivity to a number of test conditions which are difficult to precisely control and replicate.

Both the *Default* and *Compact* matrices exhibited what appeared to be a very weak coarse mode at 448nm (with a minimum beginning at about 191.1nm). Although the SMPS in this study was limited to a maximum size bin of 224.7nm, these results are very similar to those from Xue et al. (2015) for a LDD vehicle (SMPS size range 8.7-378.6nm), where the EEPS *Default* matrix appeared to measure a very weak coarse mode while neither the *Soot* matrix nor the SMPS exhibited a coarse mode. On a log-log scale (Figure 3.1), the difference between the *Soot* matrix and the other EEPS matrices for ULSD exhaust particles above 100nm is most apparent. The *Soot* matrix has a broader accumulation mode

(GSD = 1.79) relative to the *Default* matrix (GSD = 1.51), resulting in higher measured concentrations of larger (>100nm) particles.

Table 3.3 shows the peak diameter (bin midpoint with the highest average concentration) for each distribution (by instrument/matrix) along with the corresponding average PN concentration (dN/dlogDp) and one standard deviation (±σ). EEPS *Default*, *Soot*, and *Compact* concentrations were higher than the SMPS by factors of 1.9, 1.3, and 2.5, respectively. In terms of both shape and magnitude, the PSD produced with the EEPS *Soot* matrix corresponded better with the SMPS than the other two matrices.

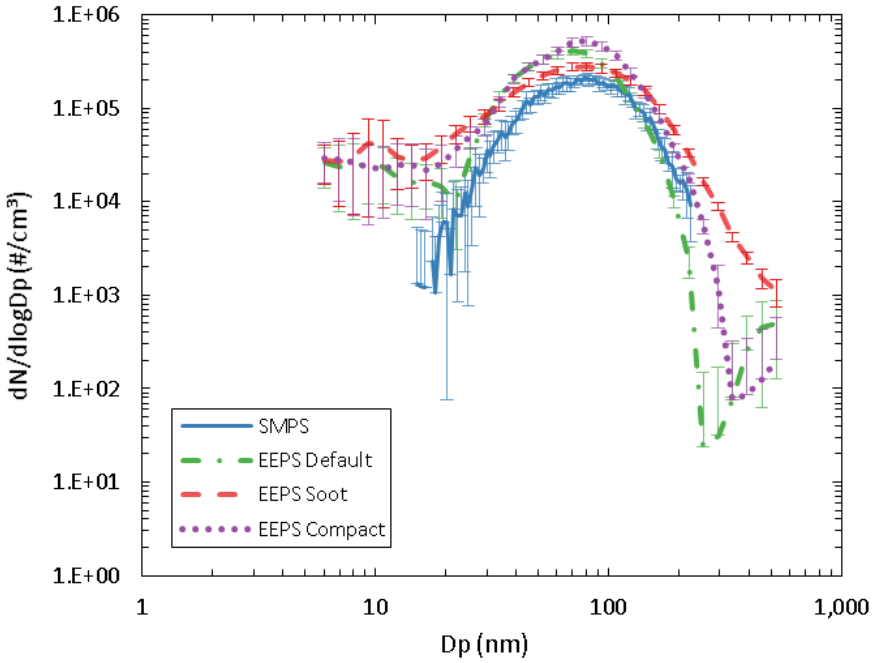


**Figure 3.1: Log-log plot of average (±σ) ULSD PSDs (75% engine load)**

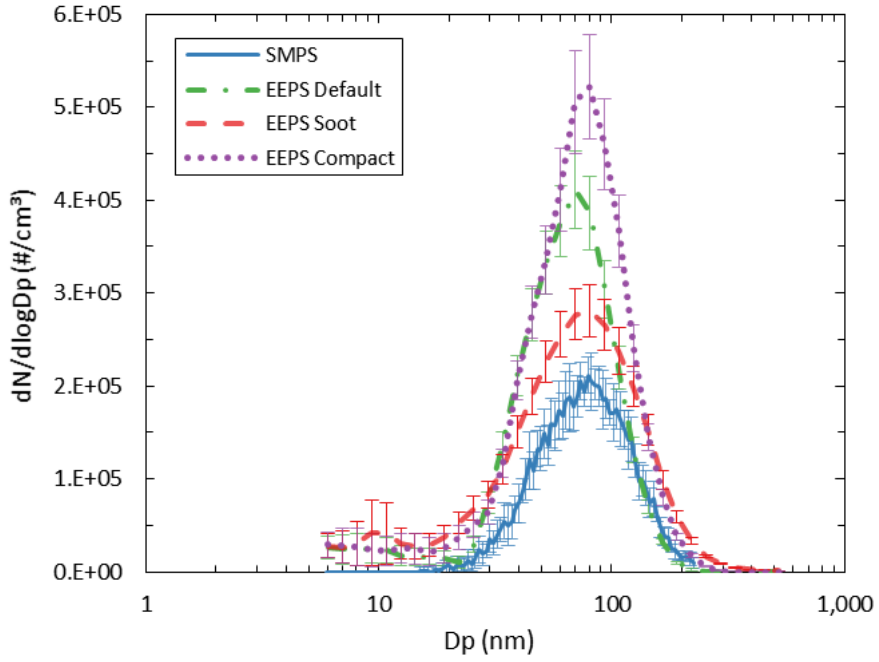


**Figure 3.2: Semi-log plot of average (±σ) ULSD PSDs (75% engine load)**

**Table 3.2: Trimodal fit parameters for lognormal ULSD PSDs by measurement method**

| | | Nucleation Mode | | | Accumulation Mode | | | Coarse Mode | | |
|---|---|---|---|---|---|---|---|---|---|---|
| | | Fraction (%) | GMD (nm) | GSD | Fraction (%) | GMD (nm) | GSD | Fraction (%) | GMD (nm) | GSD |
| | **SMPS** | — | — | — | 100 | 75 | 1.57 | — | — | — |
| **EEPS** | ***Default*** | 6 | 10 | 1.43 | 94 | 66 | 1.51 | 0.04 | 448 | 1.18 |
| | ***SOOT*** | 1 | 9 | 1.31 | 99 | 71 | 1.79 | — | — | — |
| | ***Compact*** | 5 | 10 | 1.39 | 95 | 71 | 1.58 | 0.01 | 448 | 1.17 |

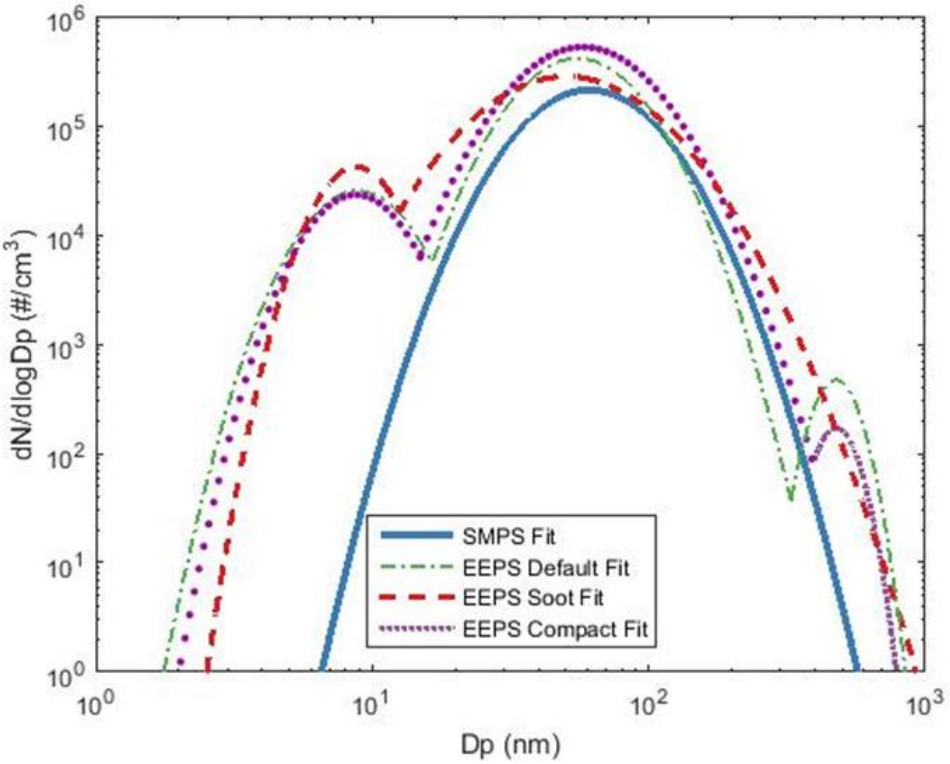


**Figure 3.3: Lognormal fits of measured ULSD PSDs**

**Table 3.3: Peak particle diameter bin size and average concentration (±σ) by measurement method for ULSD**

| | **Peak Dp Bin** (nm) | **Correspsonding dN/dlogDp** (#cm$^{-3}$ x 10$^{4}$) |
|---|---|---|
| **SMPS** | 79.1 | 2.1 ± 0.19 |
| ***Default*** | 69.8 | 4.1 ± 0.42 |
| ***SOOT*** | 80.6 | 2.8 ± 0.28 |
| ***Compact*** | 80.6 | 5.2 ± 0.57 |

### 3.2.2. Biodiesel Steady-State PSDs

Average PSDs measured by each EEPS matrix and the SMPS are shown on both a log-log plot (Figure 3.4) and semi-log plot (Figure 3.5), where vertical error bars represent one standard deviation (±σ). PSDs were fit to lognormal distributions and corresponding GMDs and GSDs are listed in Table 3.4. A log-log plot of these lognormal fits are shown in Figure 3.6. Only the accumulation mode was observed in all biodiesel exhaust PSDs in this study, which is contrary to PSDs reported by the majority of authors that often demonstrate a distinct nucleation mode (Lapuerta et al., 2008). For a diesel generator operating on biodiesel (100%), Xue et al. (2015) reported a similar distinct accumulation mode, as well as a weak nucleation mode at 11nm by both SMPS and EEPS (*Default* and *Soot*). Although the shape of the biodiesel PSDs correspond well between all instruments/matrices (Table 3.4), all three EEPS matrices demonstrate much greater magnitude than the SMPS (Table 3.5). Table 3.5 shows the peak diameter (bin midpoint with the highest average concentration) for each distribution along with the corresponding average PN concentration (dN/dlogDp) and one standard deviation (±σ). EEPS *Default*, *Soot*, and *Compact* concentrations were higher than the SMPS by factors of 2.1, 1.7, and 2.4, respectively.

Xue et al. (2015) reported good agreement between EEPS (*Default* and *Soot*) and SMPS measurements of biodiesel exhaust particles, although they did not evaluate the *Compac*t matrix. Assuming that the composition of the particles did not affect unipolar charging (Wang et al., 2016a & 2016b) this indicates that these biodiesel particles may possess a highly fractal morphology not accounted for by any of the current EEPS matrices. Contrary to many other studies on the topic, PM generated by the LDD engine used in this

study has exhibited an increasing trend in mass concentrations by biodiesel percentage used (see Appendix, Figure A.3), which may be related to the underlying reason why the results shown here differ from those reported by Xue et al. (2015) – i.e., biodiesel particles generated under certain key test conditions may have a unique or unexpected morphology, density, or chemical composition which affects their measurement via electrical mobility techniques.

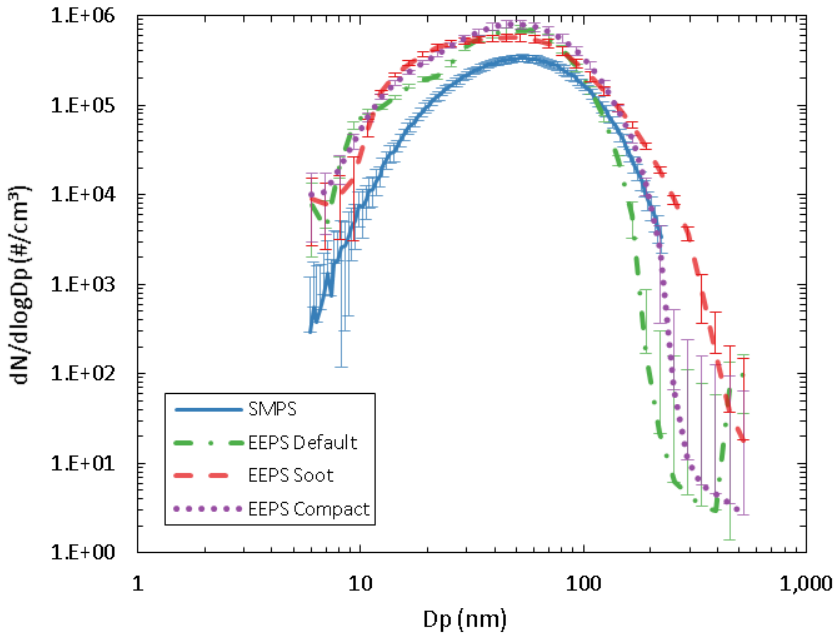


**Figure 3.4: Log-log plot of average (±σ) biodiesel PSDs (75% engine load)**

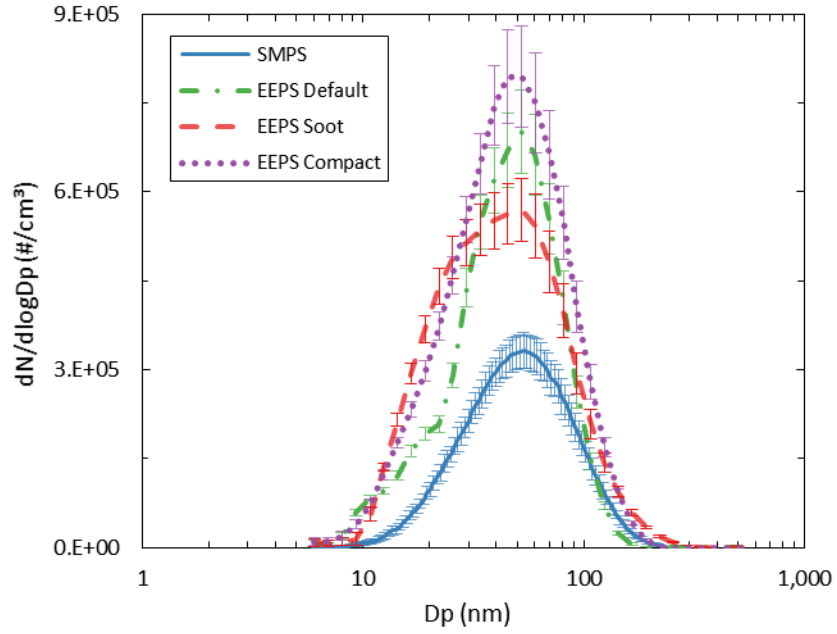


**Figure 3.5: Semi-log plot of average (±σ) biodiesel PSDs (75% engine load)**

**Table 3.4: Unimodal fit parameters for lognormal biodiesel PSDs by measurement method**

| | | **GMD** (nm) | **GSD** |
|---|---|---|---|
| | **SMPS** | 49 | 1.74 |
| **EEPS** | ***Default*** | 42 | 1.76 |
| | ***SOOT*** | 41 | 1.90 |
| | ***Compact*** | 43 | 1.83 |

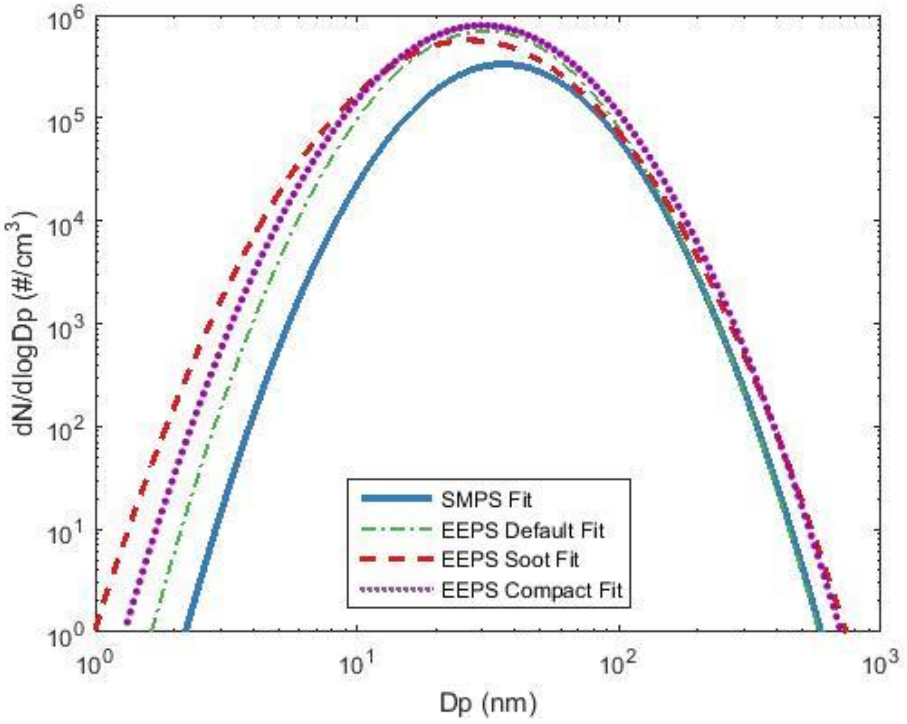


**Figure 3.6: Lognormal fits of measured biodiesel PSDs**

**Table 3.5: Peak particle diameter bin size and average concentration (±σ) by measurement method for biodiesel**

| | | **Peak Dp Bin** (nm) | **Correspsonding dN/dlogDp** (#cm$^{-3}$ x 10$^5$) |
|---|---|---|---|
| | **SMPS** | 53.3 | 3.3 ± 0.28 |
| **EEPS** | ***Default*** | 52.3 | 7.0 ± 0.70 |
| | ***SOOT*** | 52.3 | 5.7 ± 0.53 |
| | ***Compact*** | 52.3 | 7.9 ± 0.85 |

## 3.3. Comparison of PM Measurements (Gravimetric vs. IPSD)

### 3.3.1. ULSD Transient Test PM

Table 3.6 shows mass concentrations measured from the ULSD transient test. Average IPSD estimated mass concentrations are given for the same time period during which the filter sampled. The variation in these average values reflects both instrument variation and variation due to transient engine emissions. For this reason, standard deviations are not reported. The percent difference of each IPSD estimated mass concentration from the concentration measured gravimetrically are listed in Table 3.7, with differences within ±10% highlighted in yellow. In this case, PM calculated from both the *Soot* and *Compact* matrices using the *Fractal* effective density distribution were both within ±10% of the value measured gravimetrically. Although the mass estimated with the *Compact* matrix and *Fractal* $\rho$ was closest to gravimetric (within 6%), it is apparent from Figure 3.2 that this is due to an overestimation of accumulation mode particles (higher than SMPS by a factor of ~2.5) rather than a more accurate measurement of ULSD PSDs.

The EEPS *Soot* matrix not only showed the best agreement with SMPS PSD data from the ULSD steady-state test, but also agreed well with the gravimetric measurement when combined with *Fractal* $\rho$ to calculate PM mass by the IPSD method. These results support previous findings that the *Soot* matrix is currently the best available option for measurement of ULSD exhaust particles by the EEPS (Xue et al., 2015) and that particle effective density functions/distributions similar to *Fractal* $\rho$ are an accurate estimate for ULSD exhaust particles under many conditions (Park et al., 2003; Maricq & Xu, 2004).

**Table 3.6: Mass concentrations (µg/m³) measured from the ULSD transient test**

| *Gravimetric PM = 35.5 µg/m³* | | EEPS Inversion Matrix | | |
|---|---|---|---|---|
| | | Default | Soot | Compact |
| Effective Density | Unit | 39.9 | 89.8 | 73.7 |
| | Fractal | 20.5 | 32.2 | 33.4 |
| | Adsorbed | 57.1 | 125.8 | 104.8 |

**Table 3.7: Percent differences in calculated mass concentrations from gravimetric for the ULSD transient test**

| | | EEPS Inversion Matrix | | |
|---|---|---|---|---|
| | | Default | Soot | Compact |
| Effective Density | Unit | 12% | 153% | 108% |
| | Fractal | -42% | **-9%** | **-6%** |
| | Adsorbed | 61% | 254% | 195% |

Figure 3.7 shows the cumulative PM mass (estimated by IPSD with the EEPS *Soot* matrix and *Fractal ρ*) plotted against engine load. The relationship between engine load and PM mass emission rate is evident from this figure, where the slope of the plotted cumulative mass is steepest during high engine load events. This is most pronounced in the steady-state, 75% percent engine load section during the last 10 minutes of the test cycle, which, by this IPSD estimate, represented approximately 40% of the total mass collected by the filter for the entire ~95 minute emissions test.

The relationship between particle emission rates (number and mass) and engine load is explored further in the fractional contribution charts in Figure 3.8, Figure 3.9, and Figure 3.10. For each portion of the cycle (one transient and three steady state phases), the

fractional contribution by particle size range – categorized here as "nanoparticle" (<50nm), "ultrafine" (50-100nm), and "fine" (>100nm) – was determined for both total particle number (TPN) and mass (using *Fractal ρ* to estimate PM mass by IPSD). Fractional contributions for number and mass during the transient phase are shown in Figure 3.8. Fractional contributions for each steady-state condition are shown for number and mass in Figure 3.9 and Figure 3.10, respectively. All three figures compare fractional contributions by particle size for EEPS measurements exported with the *Default* and *Soot* matrices (using *Fractal ρ* to estimate PM mass by IPSD). Average values for TPN and mass concentrations are shown above the column for each condition. The trend in TPN fractional contribution by engine load in Figure 3.9 is very similar to the results reported by Betha & Balasubramanian (2011) for FMPS measurements of diesel generator exhaust, where the relative proportion of nanoparticles decreases linearly with increasing engine load.

By comparing the TPN fractional contributions for the *Default* and *Soot* matrices, it can be seen that the *Soot* matrix broadens the number-weighted PSD relative to the *Default* matrix (this is also evident in the PSD plots in Section 3.2.1). Under each condition (transient or steady-state by load) the relative contribution of the ultrafine size range is decreased and shifted to the nanoparticle and fine size ranges. The consequences of this broadened number-weighted PSD for mass estimated by the IPSD method is apparent in the mass-weighted fractional contributions, where an increase in the estimate of fine particle number results in a substantially greater increase in estimated total mass. Across all conditions, relative to the *Default* matrix, the *Soot* matrix consistently results in a factor of 1.2 (±0.12) increase in measured TPN, while the calculated (by IPSD, as stated above)

total volume and mass increase by factors of 2.19 (±0.14) and 1.55 (±0.05), respectively. In order to estimate PM mass by IPSD it is critical to accurately measure the number and estimate the density of larger particles (>50nm). As long as mass remains the regulatory metric, reliable measurement of the largest particles in the size range of interest will be most crucial to producing accurate and repeatable estimates of PM. As technology and methodology improve to increase the reliability of nanoparticle (defined here as <50nm) number measurement (a metric which may be more relevant to human health than PM mass), this may change.

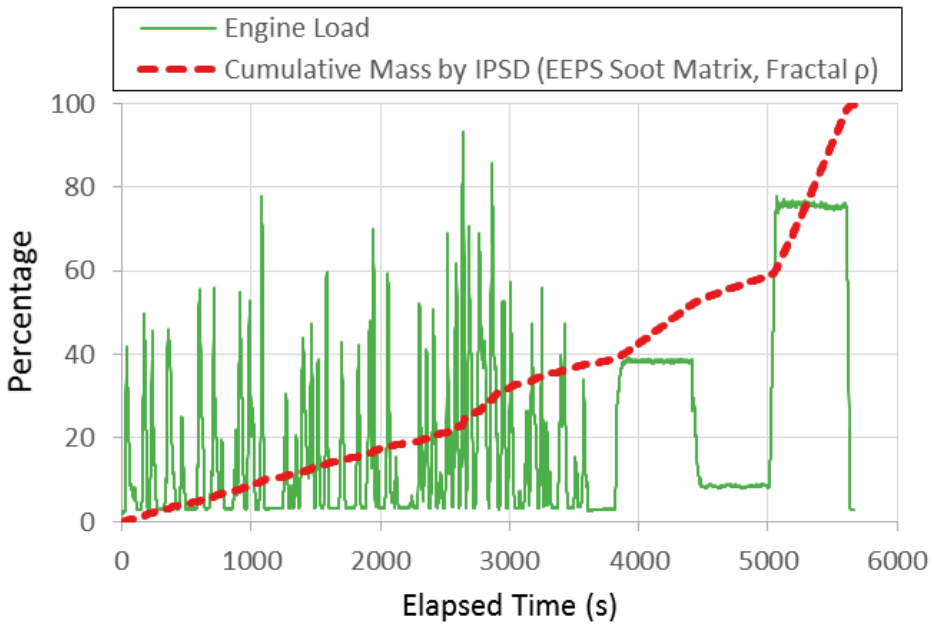


**Figure 3.7: Cumulative mass (from IPSD with EEPS *Soot Matrix* and *Fractal ρ*) vs engine load during the ULSD transient test**

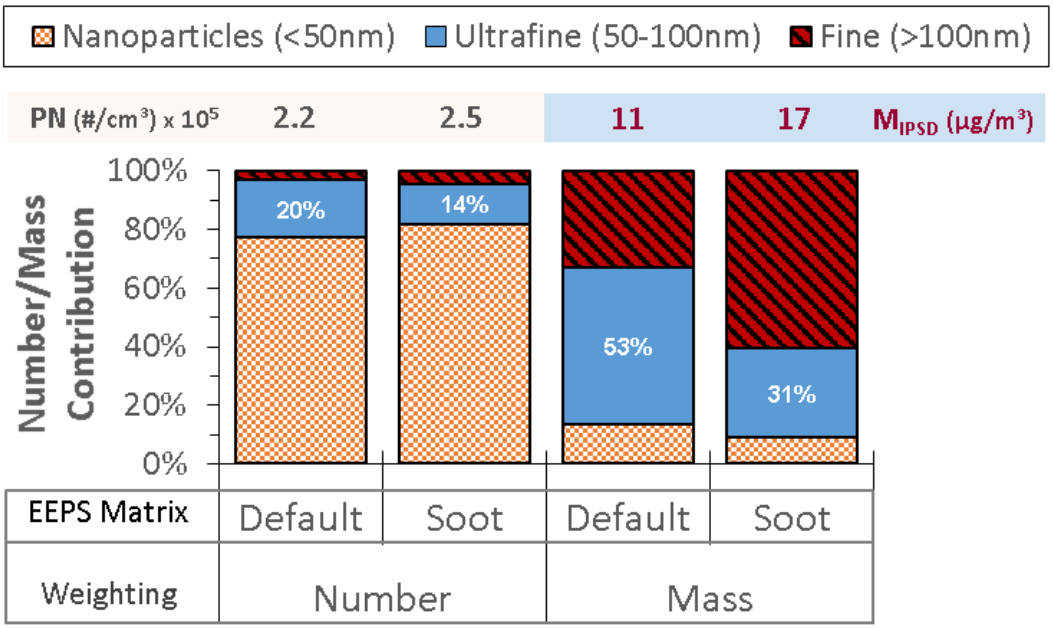


**Figure 3.8: Fractional contribution, by particle size, to number and mass (from IPSD with *Fractal ρ*) emissions during transient engine operation on ULSD**

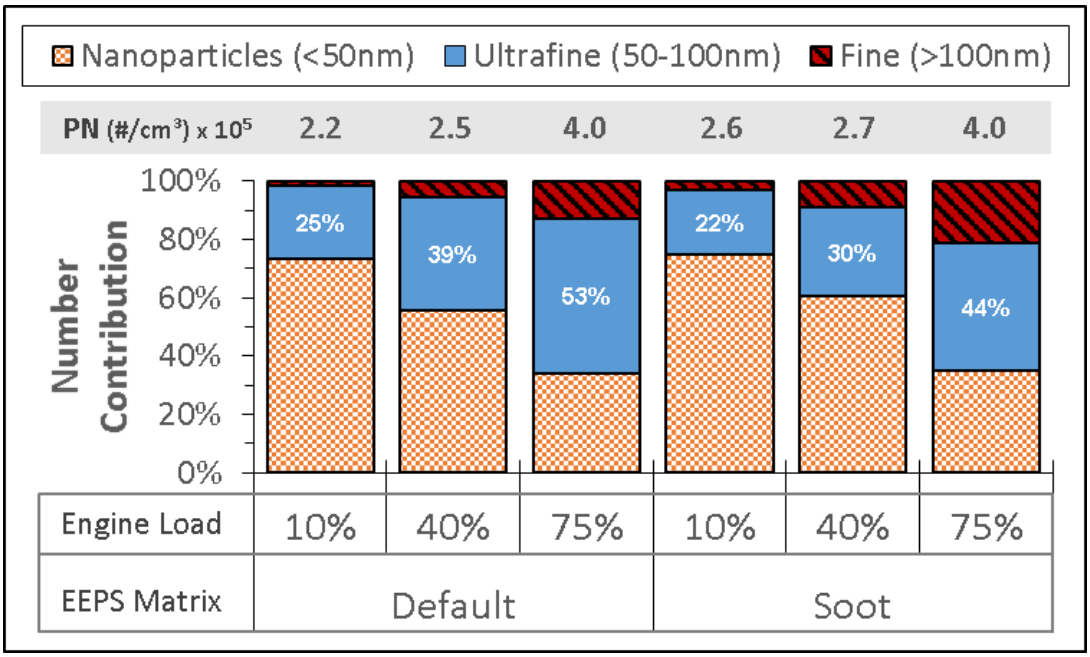


**Figure 3.9: Fractional contribution, by particle size, to number emissions by engine load on ULSD**

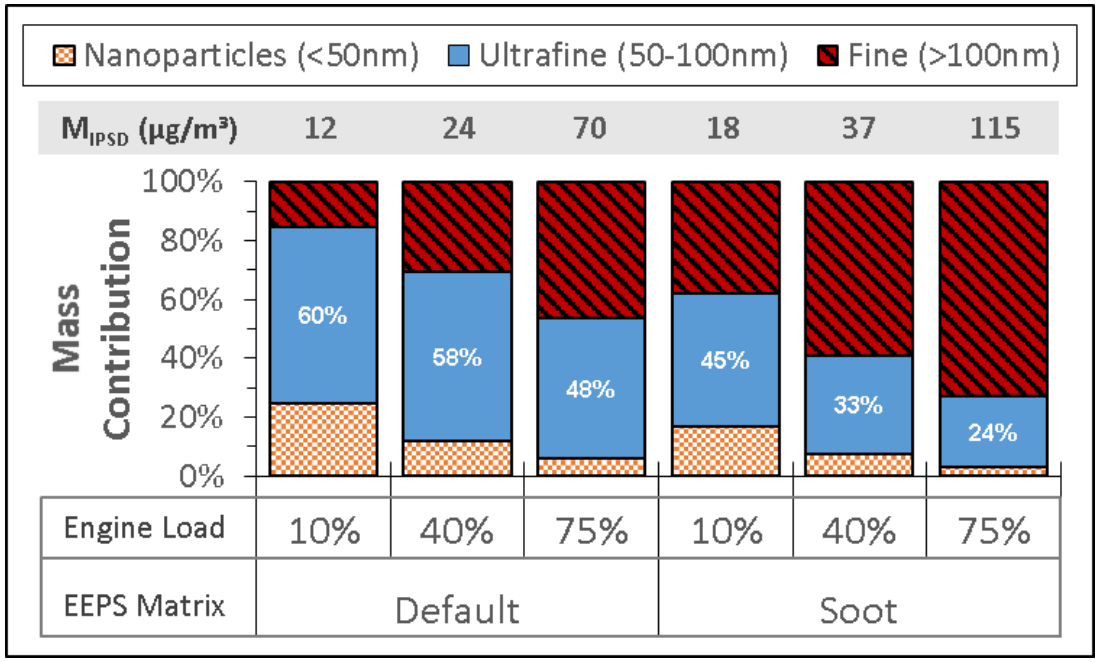


**Figure 3.10: Fractional contribution, by particle size, to mass (from IPSD with *Fractal ρ*) emissions by engine load on ULSD**

### 3.3.2. Biodiesel Steady-State PM

Table 3.8 shows mass concentrations measured from the biodiesel steady-state test. Average IPSD estimated mass concentrations, with one standard deviation (±σ), are given for the same time period during which the filter sampled. The percent difference of each IPSD estimated mass concentration from the concentration measured gravimetrically are listed in Table 3.9, with differences within ±10% highlighted in yellow. In this case, PM calculated from both the EEPS *Soot* and *Compact* matrices combined with the *Unit* effective density distribution were both within ±10% of the value measured gravimetrically. However, the interpretation of these results is very limited by the fact that none of the EEPS matrices produced PSDs which corresponded well to SMPS data for the steady-state biodiesel test, as discussed in Section 3.2.2. Without confidence in EEPS measurements of biodiesel PSDs, the accuracy of the PM values calculated from EEPS PSDs (listed in Table 3.8) cannot be verified, and instead these values mostly serve to demonstrate the sensitivity of IPSD calculated mass to differences in effective density. It should be noted that very little information is currently available regarding the effective density of biodiesel exhaust particles, and, as shown in Table 3.8, PM mass calculated from the same PSD can vary substantially (>2x here) depending on the chosen values for effective density. All of the SMPS derived estimates of PM mass underestimated the gravimetric measurement, with the closest – *Adsorbed ρ*, which has the highest values for accumulation mode particle effective density – only being within 29% of gravimetric (Table 3.9). This suggests that the accumulation mode biodiesel particles may have been even denser than particles represented by *Adsorbed ρ* – highlighting the need for research on the effective density of biodiesel particles.

**Table 3.8: Mass concentrations (µg/m³) measured from the biodiesel steady-state test**

| *Gravimetric PM = 84.5 µg/m³* | | EEPS Inversion Matrix | | | |
|---|---|---|---|---|---|
| | | Default | Soot | Compact | SMPS |
| Effective Density | Unit | 47.3 ± 4.41 | 90.4 ± 7.37 | 83.1 ± 7.38 | 42.3 ± 4.88 |
| | Fractal | 36.0 ± 3.31 | 52.5 ± 4.54 | 56.7 ± 5.23 | 27.5 ± 2.98 |
| | Adsorbed | 68.2 ± 6.34 | 128.2 ± 10.45 | 119.0 ± 10.58 | 60.4 ± 6.95 |

**Table 3.9: Percent differences in calculated mass concentrations from gravimetric for the biodiesel steady-state test**

| | | EEPS Inversion Matrix | | | |
|---|---|---|---|---|---|
| | | Default | Soot | Compact | SMPS |
| Effective Density | Unit | -44% | **7%** | **-2%** | -50% |
| | Fractal | -57% | -38% | -33% | -67% |
| | Adsorbed | -19% | 52% | 41% | -29% |

Average mass-weighted PSDs for each combination of EEPS matrix and effective density distribution are shown in a log-log plot (Figure 3.11) and semi-log plot (Figure 3.12). To facilitate visual comparison, error bars are not shown. Given the uncertainty (in this study) regarding the accuracy of the biodiesel exhaust PSDs measured and the effective density values chosen for the IPSD method, these plots are not intended to be a definite representation of mass-weighted biodiesel PSDs. Rather, Figure 3.11 and Figure 3.12 serve as a sensitivity analysis for the effect on mass estimations of choosing an appropriate combination of EEPS inversion matrix (or more generally, an accurate PSD measurement system) and values for particle effective density. From these figures it is apparent that although the *Soo*t and *Compact* matrices combined with the *Unit* effective density

distribution were both within ±10% of PM measured gravimetrically, their mass-weighted PSDs exhibit substantial differences. The potential to arrive at good agreement with a single reference measurement (gravimetric filter in this case) demonstrates that (ideally) emissions testing should require multiple supplementary particle measurement techniques which can corroborate the accuracy of each method's results (e.g., mobility, aerodynamic, and mass measurements can be checked against one another for any given test).

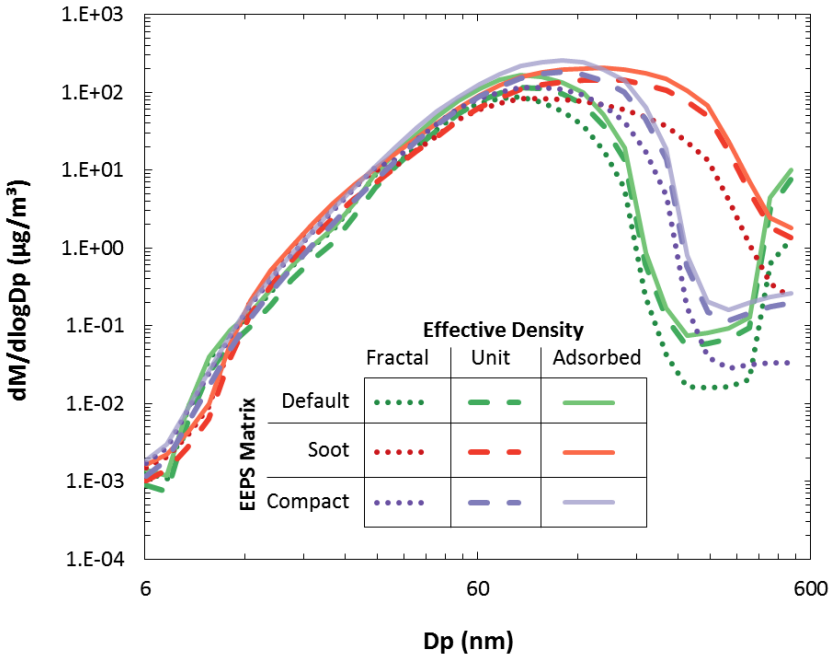


**Figure 3.11: Log-log plot of average mass-weighted biodiesel PSDs (75% engine load)**

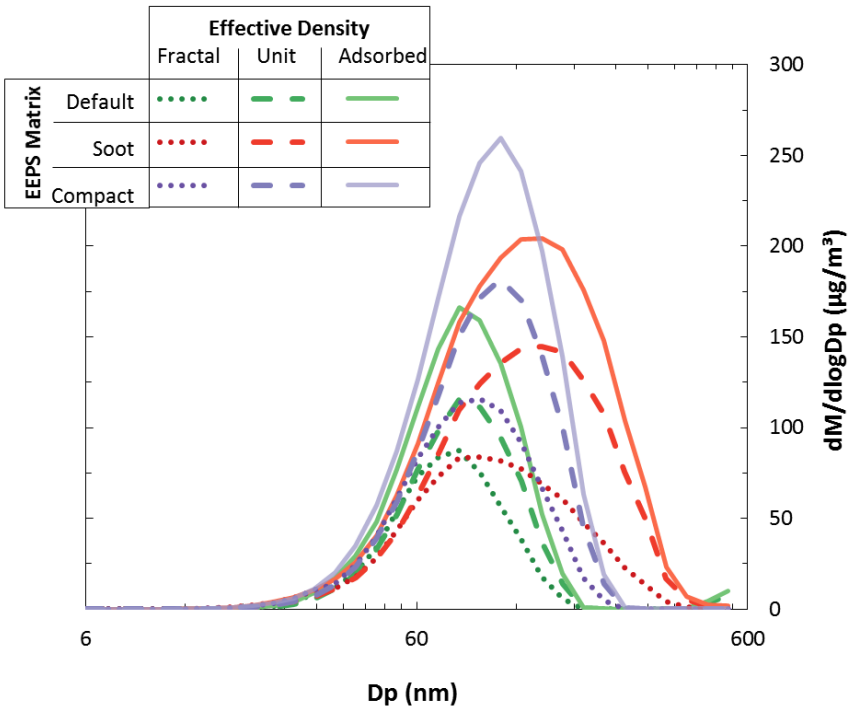


**Figure 3.12: Semi-log plot of average mass-weighted biodiesel PSDs (75% engine load)**

## CHAPTER 4: CONCLUSIONS

For both fuels (ULSD and biodiesel), all PSD measurements agreed well in terms of particle number distribution shape: primary mode (accumulation) GMD agreed within ± 10nm, and GSD agreed within ± 0.3. For ULSD, the EEPS *Default*, *Soot*, and *Compact* number concentrations at peak particle diameter were higher than the SMPS by factors of 1.9, 1.3, and 2.5, respectively. For biodiesel, EEPS *Default*, *Soot*, and *Compact* concentrations at peak particle diameter were higher than the SMPS by factors of 2.1, 1.7, and 2.4, respectively. For biodiesel exhaust, none of the three available EEPS matrices resulted in particle number distributions that corresponded well to the SMPS in terms of the magnitude of the number-weighted PSD. However, it should be noted that this statement is limited by the methods used to evaluate PSDs: shape by GMD and GSD, and magnitude by concentration at peak particle diameter. Assessment of the EEPS may have been made more conclusive with rigorous statistical analyses of PSDs. In general, the field of aerosol science would greatly benefit from the development and standardization of statistical tests for the comparison of particle size distributions. As of now, the comparison of PSDs is often done by a combination of various quantitative methods and subjective assessments.

Although additional evaluations should be conducted, the results presented here suggest that none of the EEPS calibration matrices are universally applicable to all engine/vehicle exhaust particles, including the new *Soot* matrix which was devised for this purpose. A potential solution to this issue may be that TSI implement the capability for customization of EEPS calibration matrices based on simultaneously collected SMPS and

EEPS data which can be acquired as a preliminary quality control measure by users. Also, while it may be impractical to determine specific empirical values of size-dependent effective density for each application of the IPSD method (e.g., in each unique emissions test), it may be advisable for users to at least calculate a range of IPSD estimated PM mass values utilizing sets of effective density distributions which represent the anticipated range of effective density values that may be encountered.

As an extension of this study, future work could examine EEPS measurements of biodiesel exhaust particles for blends of biodiesel and ULSD under various operating conditions. Additionally, chemical analysis (e.g., EC:OC ratio) of the PM generated, collected, and measured gravimetrically from similar tests with this CM-12 engine (see Appendix, Figure A.3) could be conducted in order to investigate whether the chemical composition of the particles may have affected electrical mobility measurement. Lastly, there is currently a lack of data on the effective density of particles produced from biodiesel and its blends with ULSD. Such data would be immensely useful towards a number of applications, including the IPSD method.

Overall, this work represents mixed results for the viability of the IPSD method for the estimation of gravimetric PM. In general, great strides have been taken in the endeavor to measure engine exhaust particles for regulatory purposes, including technical innovations such as the EEPS and a growing foundation of knowledge regarding particle characteristics (e.g., effective density). However, each discovery and success is often the progenitor of future questions and potential problems. In this case, the benefits associated with the applications of biodiesel and the IPSD method have exposed our current lack of

knowledge regarding the properties of biodiesel exhaust particles as well as the need to continue to advance and refine aerosol measurement capabilities.

## REFERENCES CITED


Abdul-Khalek, I. S., Kittelson, D. B., Graskow, B. R., Wei, Q., & Bear, F. (1998). "Diesel exhaust particle size: measurement issues and trends" (No. 980525). *SAE Technical Paper*.

Bakeas, E., Karavalakis, G., & Stournas, S. (2011). "Biodiesel emissions profile in modern diesel vehicles. Part 1: Effect of biodiesel origin on the criteria emissions." *Science of the Total Environment*, 409(9), pp.1670-1676.

Bakeas, E., Karavalakis, G., Fontaras, G., & Stournas, S. (2011). "An experimental study on the impact of biodiesel origin on the regulated and PAH emissions from a Euro 4 light-duty vehicle." *Fuel*, 90(11), pp.3200-3208.

Bannister, C.D., Hawley, J.G., Ali, H.M., Chuck, C.J., Price, P., Chrysafi, S.S., Brown, A., & Pickford, W. (2010). "The impact of biodiesel blend ratio on vehicle performance and emissions." *Proceedings of the Institution of Mechanical Engineers, Part D: Journal of Automobile Engineering*, 224(3), pp.405-421.

Betha, R., & Balasubramanian, R. (2011). "Particulate emissions from a stationary engine fueled with ultra-low-sulfur diesel and waste-cooking-oil-derived biodiesel." *Journal of the Air & Waste Management Association*, 61(10), pp.1063-1069.

Bielaczyc, P., & Szczotka, A. (2008). "A study of RME-based biodiesel blend influence on performance, reliability and emissions from modern light-duty diesel engines" (No. 2008-01-1398*). SAE Technical Paper*.

Bielaczyc, P., Szczotka, A., Gizynski, P., & Bedyk, I. (2009). "The effect of pure RME and biodiesel blends with high RME content on exhaust emissions from a light duty diesel engine" (No. 2009-01-2653). *SAE Technical Paper*.

Chung, A., Lall, A. A., & Paulson, S. E. (2008). "Particulate emissions by a small non-road diesel engine: Biodiesel and diesel characterization and mass measurements using the extended idealized aggregates theory." *Atmospheric Environment*, 42(9), pp.2129-2140.

Dastanpour, R., & Rogak, S. N. (2016). "The effect of primary particle polydispersity on the morphology and mobility diameter of the fractal agglomerates in different flow regimes." *Journal of Aerosol Science*, 94, pp.22-32.

DeCarlo, P. F., Slowik, J. G., Worsnop, D. R., Davidovits, P., & Jimenez, J. L. (2004). "Particle morphology and density characterization by combined mobility and aerodynamic diameter measurements. Part 1: Theory." *Aerosol Science and Technology*, 38(12), pp.1185-1205.

EPA. (2002). “A Comprehensive Analysis of Biodiesel Impacts on Exhaust Emissions” (EPA420-P-02-001). *United States Environmental Protection Agency*.

EPA. (2009). “Integrated Science Assessment for Particulate Matter” (EPA600-R-08-139F). *United States Environmental Protection Agency*.

Flagan, R. C. (2001). "Electrical techniques." *Aerosol Measurement: Principles, Techniques, and Applications*, pp.537-568.

Fontaras, G., Karavalakis, G., Kousoulidou, M., Tzamkiozis, T., Ntziachristos, L., Bakeas, E., Stournas, S., & Samaras, Z. (2009). “Effects of biodiesel on passenger car fuel consumption, regulated and non-regulated pollutant emissions over legislated and real-world driving cycles.” *Fuel*, 88(9), pp.1608-1617.

Friedlander, S. K. (2000). *Smoke, Dust and Haze. Fundamentals of Aerosol Dynamics*. Oxford University Press, New York

Giakoumis, E.G. (2012). “A statistical investigation of biodiesel effects on regulated exhaust emissions during transient cycles.” *Applied Energy*, 98, pp.273-291.

Giechaskiel, B., Maricq, M., Ntziachristos, L., Dardiotis, C., Wang, X., Axmann, H., Bergmann, A., & Schindler, W. (2014). “Review of motor vehicle particulate emissions sampling and measurement: From smoke and filter mass to particle number.” *Journal of Aerosol Science*, 67, pp.48-86.

Guha, S., Li, M., Tarlov, M.J., & Zachariah, M.R. (2012). “Electrospray–differential mobility analysis of bionanoparticles.” *Trends in Biotechnology*, 30(5), pp.291-300.

Hamra, G.B., Guha, N., Cohen, A., Laden, F., Raaschou-Nielsen, O., Samet, J.M., Vineis, P., Forastiere, F., Saldiva, P., Yorifuji, T., & Loomis, D. (2014). “Outdoor particulate matter exposure and lung cancer: a systematic review and meta-analysis.”

Harris, S.J., & Maricq, M.M. (2002). “The role of fragmentation in defining the signature size distribution of diesel soot.” *Journal of Aerosol Science*, 33(6), pp.935-942.

Heywood, J.B. (1998). *Internal Combustion Engine Fundamentals*. McGraw-Hill, New York.

Hinds, W.C. (1999). *Aerosol Technology: Properties, Behavior, and Measurement of Airborne Particles*, 2nd edition. John Wiley & Sons, New York.

Hoekman, S. K., Broch, A., Robbins, C., Ceniceros, E., & Natarajan, M. (2012). “Review of biodiesel composition, properties, and specifications.” *Renewable and Sustainable Energy Reviews*, 16(1), pp.143-169.

Holmén, B.A., Feralio, T., Dunshee, J., & Sentoff, K (2014). “Tailpipe Emissions and Engine Performance of a Light-Duty Diesel Engine Operating on Petro- and Bio-diesel Fuel Blends” (No. TRC Report 14-008).

Hwang, J., Jung, Y., & Bae, C. (2015). “Comprehensive assessment of soot particles from waste cooking oil biodiesel and diesel in a compression ignition engine.” *SAE International Journal of Fuels and Lubricants*, 8(2), pp.290-297.

International Agency for Research on Cancer. (2012)."IARC: Diesel engine exhaust carcinogenic." *Press Release*, (213).

Karavalakis, G., Stournas, S., Ampatzoglou, D., Bakeas, E., & Spanos, A. (2010). “Regulated and unregulated emissions of a Euro 4 SUV operated with diesel and soy-based biodiesel blends.” *SAE International Journal of Fuels and Lubricants*, 2(2), pp.115-131.

Karavalakis, G., Bakeas, E., Fontaras, G., & Stournas, S. (2011). “Effect of biodiesel origin on regulated and particle-bound PAH (polycyclic aromatic hydrocarbon) emissions from a Euro 4 passenger car.: *Energy*, 36(8), pp.5328-5337.

Kasper, G. (1982). “Dynamics and measurement of smokes. I Size characterization of nonspherical particles.” *Aerosol Science and Technology*, 1(2), pp.187-199.

Kasumba, J. (2015) "Organic Chemical Characterization of Primary and Secondary Biodiesel Exhaust Particulate Matter" (Doctoral Dissertation, The University of Vermont).

Kittelson, D.B. (1998). “Engines and nanoparticles: a review.” *Journal of Aerosol Science*, 29(5), pp.575-588.

Knutson, E.O., & Whitby, K.T. (1975). “Aerosol classification by electric mobility: apparatus, theory, and applications.” *Journal of Aerosol Science*, 6(6), pp.443-451.

Kousoulidou, M., Fontaras, G., Ntziachristos, L., & Samaras, Z. (2009). “Evaluation of biodiesel blends on the performance and emissions of a common-rail light-duty engine and vehicle” (No. 2009-01-0692). *SAE Technical Paper*.

Kulkarni, P., Baron, P.A., & Willeke, K., editors. (2011). *Aerosol Measurement: Principles, Techniques, and Applications*. John Wiley & Sons, New York.

Lapuerta, M., Armas, O., & Rodriguez-Fernandez, J. (2008). “Effect of biodiesel fuels on diesel engine emissions.” *Progress in Energy and Combustion science*, 34(2), pp.198-223.

Li, Y., Xue, J., Johnson, K., Durbin, T., Villela, M., Pham, L., Hosseini, S., Zheng, Z., Short, D., Karavalakis, G., & Asa-Awuku, A. (2014). "Determination of suspended exhaust PM mass for light-duty vehicles." *SAE Technical Paper*, pp.01-1594.

Liu, Z.G., Vasys, V.N., Dettmann, M.E., Schauer, J.J., Kittelson, D.B., & Swanson, J. (2009). "Comparison of strategies for the measurement of mass emissions from diesel engines emitting ultra-low levels of particulate matter." *Aerosol Science and Technology*, 43(11), pp.1142-1152.

Maricq, M.M., & Xu, N. (2004). "The effective density and fractal dimension of soot particles from premixed flames and motor vehicle exhaust." *Journal of Aerosol Science*, 35(10), pp.1251-1274.

Martini, G., Astorga, C., & Farfaletti, A. (2007). "Effect of biodiesel fuels on pollutant emissions from EURO 3 LD diesel vehicles." *European Commission Joint Research Center, Institute for Environment and Sustainability*, EUR 22745.

Merchan-Merchan, W., Sanmiguel, S.G., & McCollam, S. (2012). "Analysis of soot particles derived from biodiesels and diesel fuel air-flames." *Fuel*, 102, pp.525-535.

Park, K., Cao, F., Kittelson, D.B., & McMurry, P.H. (2003). "Relationship between particle mass and mobility for diesel exhaust particles." *Environmental Science & Technology*, 37(3), pp.577-583.

Quiros, D.C., Hu, S., Hu, S., Lee, E.S., Sardar, S., Wang, X., Olfert, J.S., Jung, H.S., Zhu, Y., & Huai, T. (2015a). "Particle effective density and mass during steady-state operation of GDI, PFI, and diesel passenger cars." *Journal of Aerosol Science*, 83, pp.39-54.

Quiros, D.C., Zhang, S., Sardar, S., Kamboures, M.A., Eiges, D., Zhang, M., Jung, H.S., Mccarthy, M.J., Chang, M.C.O., Ayala, A., & Zhu, Y. (2015b). "Measuring Particulate Emissions of Light Duty Passenger Vehicles Using Integrated Particle Size Distribution (IPSD)." *Environmental Science & Technology*, 49(9), pp.5618-5627.

Ristovski, Z.D., Miljevic, B., Surawski, N.C., Morawska, L., Fong, K.M., Goh, F., & Yang, I.A. (2012). "Respiratory health effects of diesel particulate matter." *Respirology*, 17(2), pp.201-212.

Robinson, A.L., Grieshop, A.P., Donahue, N.M., & Hunt, S.W. (2010). "Updating the conceptual model for fine particle mass emissions from combustion systems." *Journal of the Air & Waste Management Association*, 60(10), pp.1204-1222.

Rushton, L. (2012). "The problem with diesel." *Journal of the National Cancer Institute*, 104(11), pp.796-797.

Schauer, J.J., Kleeman, M.J., Cass, G.R., & Simoneit, B.R. (1999). "Measurement of emissions from air pollution sources. 2. C1 through C30 organic compounds from medium duty diesel trucks." *Environmental Science & Technology*, 33(10), pp.1578-1587.

Seinfeld J. H., & Pandis S. N. (1998). *Atmospheric Chemistry and Physics: From Air Pollution to Climate Change*, 1st edition. John Wiley & Sons, New York.

Shin, W.G., Qi, C., Wang, J., Fissan, H., & Pui, D.Y. (2009). "The effect of dielectric constant of materials on unipolar diffusion charging of nanoparticles." *Journal of Aerosol Science*, 40(5), pp.463-468.

Shin, W.G., Wang, J., Mertler, M., Sachweh, B., Fissan, H., & Pui, D.Y. (2010). "The effect of particle morphology on unipolar diffusion charging of nanoparticle agglomerates in the transition regime." *Journal of Aerosol Science*, 41(11), pp.975-986.

Smekens, A., Godoi, R.H.M., Berghmans, P., & Van Grieken, R. (2005). "Characterisation of soot emitted by domestic heating, aircraft and cars using diesel or biodiesel." *Journal of Atmospheric Chemistry*, 52(1), pp.45-62.

Surawski, N.C., Miljevic, B., Ayoko, G.A., Elbagir, S., Stevanovic, S., Fairfull-Smith, K.E., Bottle, S.E., & Ristovski, Z.D. (2011). "Physicochemical characterization of particulate emissions from a compression ignition engine: The influence of biodiesel feedstock." *Environmental Science & Technology*, 45(24), pp.10337-10343.

Swanson, J., Kittelson, D., & Dikken, D. (2009). "Uncertainties in filter mass measurements made to determine compliance with the 2007 diesel PM standard." *SAE International Journal of Fuels and Lubricants*, 2(1), pp.708-717.

Symonds, J.P., Reavell, K.S.J., Olfert, J.S., Campbell, B.W., & Swift, S.J. (2007). "Diesel soot mass calculation in real-time with a differential mobility spectrometer." *Journal of Aerosol Science*, 38(1), pp.52-68.

Tinsdale, M., Price, P., & Chen, R. (2010). "The impact of biodiesel on particle number, size and mass emissions from a Euro4 diesel vehicle."

TSI. (2006). "Model 3090 Engine Exhaust Particle Sizer Spectrometer operation and service manual."

TSI. (2015). APPLICATION NOTE EEPS-005 (A4): "Updated inversion matrices for engine exhaust particle sizer (EEPS) spectrometer model 3090."

Tsolakis, A., Megaritis, A., Wyszynski, M.L., & Theinnoi, K. (2007). "Engine performance and emissions of a diesel engine operating on diesel-RME (rapeseed methyl ester) blends with EGR (exhaust gas recirculation)." *Energy*, 32(11), pp.2072-2080.

Twigg, M.V., & Phillips, P.R. (2009). "Cleaning the air we breathe-Controlling diesel particulate emissions from passenger cars." *Platinum Metals Review*, 53(1), pp.27-34.

Tzamkiozis, T., Ntziachristos, L., Mamakos, A., Fontaras, G., & Samaras, Z. (2011). "Aerodynamic and mobility size distribution measurements to reveal biodiesel effects on diesel exhaust aerosol." *Aerosol Science and Technology*, 45(5), pp.587-595.

Vouitsis, E., Ntziachristos, L., & Samaras, Z. (2003). "Particulate matter mass measurements for low emitting diesel powered vehicles: what's next?" *Progress in Energy and Combustion Science*, 29(6), pp.635-672.

Vu, D., Short, D., Karavalakis, G., Durbin, T.D., & Asa-Awuku, A. (2015). "Integrating Cloud Condensation Nuclei Predictions with Fast Time Resolved Aerosol Instrumentation to Determine the Hygroscopic Properties of Emissions Over Transient Drive Cycles." *Aerosol Science and Technology*, 49(11), pp.1149-1159.

Wang, X., Grose, M.A., Avenido, A., Stolzenburg, M.R., Caldow, R., Osmondson, B.L., Chow, J.C., & Watson, J.G. (2016a). "Improvement of Engine Exhaust Particle Sizer (EEPS) size distribution measurement–I. Algorithm and applications to compact-shape particles." *Journal of Aerosol Science*, 92, pp.95-108.

Wang, X., Grose, M.A., Caldow, R., Osmondson, B.L., Swanson, J.J., Chow, J.C., Watson, J.G., Kittelson, D.B., Li, Y., Xue, J., & Jung, H. (2016b). "Improvement of Engine Exhaust Particle Sizer (EEPS) size distribution measurement–II. Engine exhaust particles." *Journal of Aerosol Science*, 92, pp.83-94.

Weber, R. (2015). *Class Resources: EAS 6430 Graduate Lab*. Georgia Institute of Technology; Atlanta, GA.

Wu, F., Wang, J., Chen, W., & Shuai, S. (2009). "A study on emission performance of a diesel engine fueled with five typical methyl ester biodiesels." *Atmospheric Environment*, 43(7), pp.1481-1485.

Xue, J. (2013). "Combustion characteristics, engine performances and emissions of waste edible oil biodiesel in diesel engine." *Renewable and Sustainable Energy Reviews*, 23, pp.350-365.

Xue, J., Li, Y., Wang, X., Durbin, T.D., Johnson, K.C., Karavalakis, G., Asa-Awuku, A., Villela, M., Quiros, D., Hu, S., & Huai, T. (2015). "Comparison of vehicle exhaust particle size distributions measured by SMPS and EEPS during steady-state conditions." *Aerosol Science and Technology*, 49(10), pp.984-996.

Ye, P. (2011). "Investigation of impact of fuel injection strategy and biodiesel fueling on engine emissions and performance" (Doctoral Dissertation, The Pennsylvania State University).

Yehliu, K. (2010). "Impacts of fuel formulation and engine operating parameters on the nanostructure and reactivity of diesel soot" (Doctoral Dissertation, The Pennsylvania State University).

Zhang, J., He, K., Shi, X., & Zhao, Y. (2011). "Comparison of particle emissions from an engine operating on biodiesel and petroleum diesel." *Fuel*, 90(6), pp.2089-2097.

Zheng, Z., Johnson, K.C., Liu, Z., Durbin, T.D., Hu, S., Huai, T., Kittelson, D.B., & Jung, H.S. (2011). "Investigation of solid particle number measurement: existence and nature of sub-23nm particles under PMP methodology." *Journal of Aerosol Science*, 42(12), pp.883-897.

Zimmerman, N., Pollitt, K.J.G., Jeong, C.H., Wang, J.M., Jung, T., Cooper, J.M., Wallace, J.S., & Evans, G.J. (2014). "Comparison of three nanoparticle sizing instruments: The influence of particle morphology." *Atmospheric Environment*, 86, pp.140-147.

# APPENDICES

## A.1. Quality Assurance Results

Average total particle number (TPN) concentrations (± one standard deviation) measured by the SMPS for the steady-state tests are shown in Table A.1 (units are #/cm³). Box plots of the EEPS blank TPN concentration data - exported with all three matrices - are shown in Figure A.1 (where "preIB" refers to the instrument blank collected before engine start). All blank TPN concentrations (EEPS and SMPS) were approximately one order of magnitude (or more) lower than those measured from engine exhaust. Values for the *Soot* and *Compact* matrices exhibited greater magnitude and variation than those for the *Default* EEPS matrix.

EEPS electrometers were zeroed before each preIB and after each postIB and the offset values were saved and checked against the limits specified in the instrument manual in order to verify that electrometer currents did not drift over time. Figure A.2 displays average EEPS *Default* matrix PSDs (± one standard deviation at each size bin) for instrument blanks collected prior to data collection (preIBs) for each test. All values are near or below the instrument's detection limits and demonstrate that all particle sizes were being measured as expected by the EEPS.

**Table A.1: SMPS blank data for ULSD and biodiesel steady-state tests (#/cm³)**

| | pre-Test | | *Min. Value* | post-Test | |
|---|---|---|---|---|---|
| | Instrument Blank | Tunnel Blank | *From Test* | Tunnel Blank | Instrument Blank |
| ULSD | 10.8 ± 17.1 | 34.2 ± 13.7 | $9.8 \times 10^{3}$ | 43.3 ± 123.3 | 0 ± 0 |
| Biodiesel | 4.8 ± 4.3 | 7.4 ± 10.1 | $1.6 \times 10^{5}$ | 44.4 ± 84.0 | 8.4 ± 10.4 |

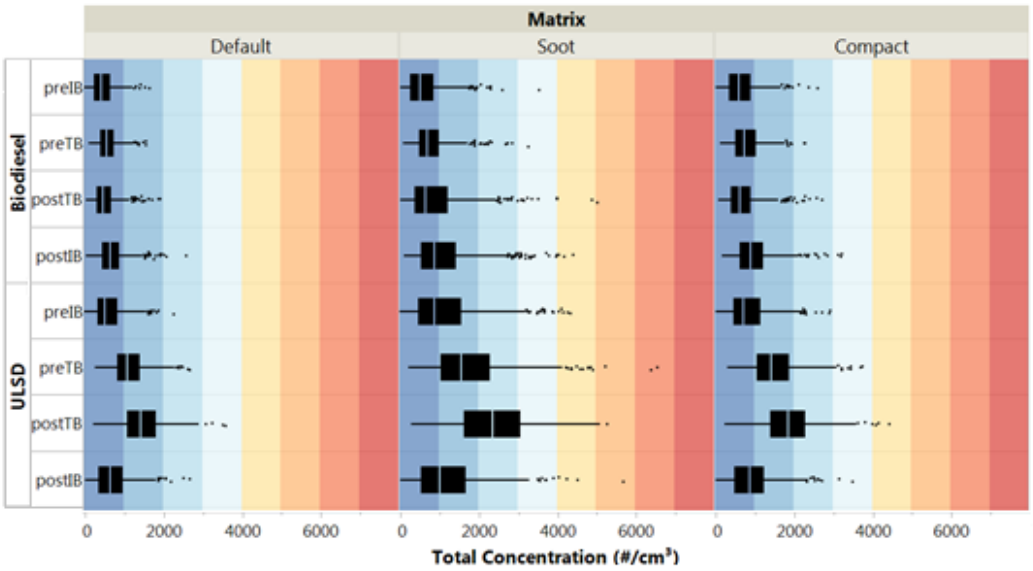


**Figure A.1: Box plots of EEPS blank data**

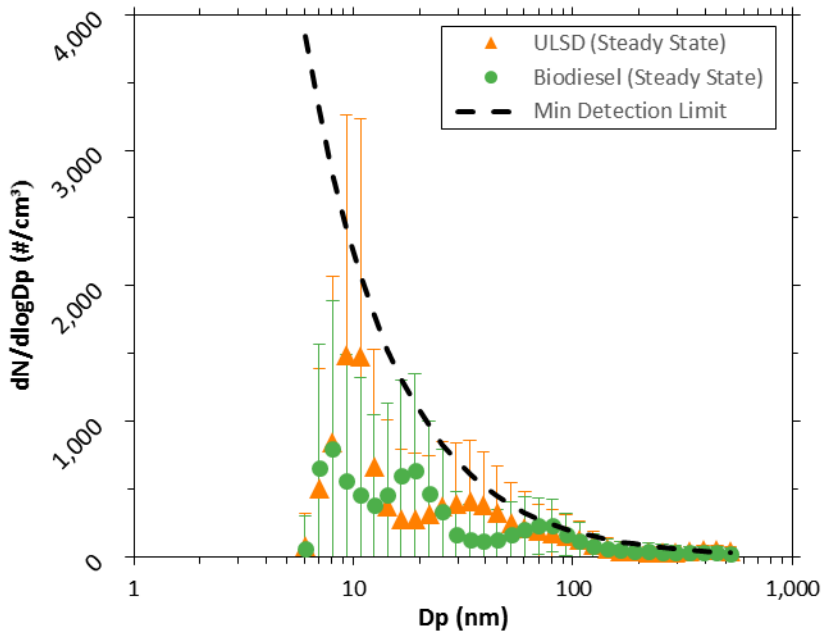


**Figure A.2: Average EEPS preIB PSDs (±σ) relative to minimum detection limit**

## A.2. EEPS and SMPS Bin Designations

**Table A.2: Engine Exhaust Particle Sizer (Model 3090) bin designations**

| Bin Number | Bin Min $D_p$ (nm) | Bin Midpoint $D_p$ (nm) | Bin Max $D_p$ (nm) |
|---|---|---|---|
| **B1** | 5.61 | 6.04 | 6.48 |
| **B2** | 6.48 | 6.98 | 7.48 |
| **B3** | 7.48 | 8.06 | 8.64 |
| **B4** | 8.64 | 9.31 | 9.98 |
| **B5** | 9.98 | 10.75 | 11.52 |
| **B6** | 11.52 | 12.41 | 13.3 |
| **B7** | 13.3 | 14.33 | 15.36 |
| **B8** | 15.36 | 16.55 | 17.74 |
| **B9** | 17.74 | 19.11 | 20.48 |
| **B10** | 20.48 | 22.07 | 23.65 |
| **B11** | 23.65 | 25.48 | 27.31 |
| **B12** | 27.31 | 29.43 | 31.54 |
| **B13** | 31.54 | 33.98 | 36.42 |
| **B14** | 36.42 | 39.24 | 42.06 |
| **B15** | 42.06 | 45.32 | 48.57 |
| **B16** | 48.57 | 52.33 | 56.09 |
| **B17** | 56.09 | 60.43 | 64.77 |
| **B18** | 64.77 | 69.78 | 74.79 |
| **B19** | 74.79 | 80.58 | 86.37 |
| **B20** | 86.37 | 93.06 | 99.74 |
| **B21** | 99.74 | 107.46 | 115.18 |
| **B22** | 115.18 | 124.09 | 133 |
| **B23** | 133 | 143.3 | 153.59 |
| **B24** | 153.59 | 165.48 | 177.37 |
| **B25** | 177.37 | 191.1 | 204.82 |
| **B26** | 204.82 | 220.67 | 236.52 |
| **B27** | 236.52 | 254.83 | 273.13 |
| **B28** | 273.13 | 294.27 | 315.41 |
| **B29** | 315.41 | 339.82 | 364.23 |
| **B30** | 364.23 | 392.42 | 420.61 |
| **B31** | 420.61 | 453.16 | 485.71 |
| **B32** | 485.71 | 523.3 | 560.89 |

**Table A.3: Scanning Mobility Particle Sizer (Model 3936) bin designations for settings in this study**

| Bin Number | Bin Min $D_p$ (nm) | Bin Mid $D_p$ (nm) | Bin Max $D_p$ (nm) | Bin Number | Bin Min $D_p$ (nm) | Bin Mid $D_p$ (nm) | Bin Max $D_p$ (nm) |
|---|---|---|---|---|---|---|---|
| **B1** | 5.83 | 5.94 | 6.04 | **B52** | 36.52 | 37.2 | 37.86 |
| **B2** | 6.04 | 6.15 | 6.26 | **B53** | 37.86 | 38.5 | 39.24 |
| **B3** | 6.26 | 6.38 | 6.49 | **B54** | 39.24 | 40 | 40.68 |
| **B4** | 6.49 | 6.61 | 6.73 | **B55** | 40.68 | 41.4 | 42.17 |
| **B5** | 6.73 | 6.85 | 6.98 | **B56** | 42.17 | 42.9 | 43.71 |
| **B6** | 6.98 | 7.1 | 7.23 | **B57** | 43.71 | 44.5 | 45.32 |
| **B7** | 7.23 | 7.37 | 7.50 | **B58** | 45.32 | 46.1 | 46.98 |
| **B8** | 7.50 | 7.64 | 7.77 | **B59** | 46.98 | 47.8 | 48.70 |
| **B9** | 7.77 | 7.91 | 8.06 | **B60** | 48.70 | 49.6 | 50.48 |
| **B10** | 8.06 | 8.2 | 8.35 | **B61** | 50.48 | 51.4 | 52.33 |
| **B11** | 8.35 | 8.51 | 8.66 | **B62** | 52.33 | 53.3 | 54.25 |
| **B12** | 8.66 | 8.82 | 8.98 | **B63** | 54.25 | 55.2 | 56.23 |
| **B13** | 8.98 | 9.14 | 9.31 | **B64** | 56.23 | 57.3 | 58.29 |
| **B14** | 9.31 | 9.47 | 9.65 | **B65** | 58.29 | 59.4 | 60.43 |
| **B15** | 9.65 | 9.82 | 10.00 | **B66** | 60.43 | 61.5 | 62.64 |
| **B16** | 10.00 | 10.2 | 10.37 | **B67** | 62.64 | 63.8 | 64.94 |
| **B17** | 10.37 | 10.6 | 10.75 | **B68** | 64.94 | 66.1 | 67.32 |
| **B18** | 10.75 | 10.9 | 11.14 | **B69** | 67.32 | 68.5 | 69.78 |
| **B19** | 11.14 | 11.3 | 11.55 | **B70** | 69.78 | 71 | 72.34 |
| **B20** | 11.55 | 11.8 | 11.97 | **B71** | 72.34 | 73.7 | 74.99 |
| **B21** | 11.97 | 12.2 | 12.41 | **B72** | 74.99 | 76.4 | 77.74 |
| **B22** | 12.41 | 12.6 | 12.86 | **B73** | 77.74 | 79.1 | 80.58 |
| **B23** | 12.86 | 13.1 | 13.34 | **B74** | 80.58 | 82 | 83.54 |
| **B24** | 13.34 | 13.6 | 13.82 | **B75** | 83.54 | 85.1 | 86.60 |
| **B25** | 13.82 | 14.1 | 14.33 | **B76** | 86.60 | 88.2 | 89.77 |
| **B26** | 14.33 | 14.6 | 14.86 | **B77** | 89.77 | 91.4 | 93.06 |
| **B27** | 14.86 | 15.1 | 15.40 | **B78** | 93.06 | 94.7 | 96.47 |
| **B28** | 15.40 | 15.7 | 15.96 | **B79** | 96.47 | 98.2 | 100.00 |
| **B29** | 15.96 | 16.3 | 16.55 | **B80** | 100.00 | 101.8 | 103.66 |
| **B30** | 16.55 | 16.8 | 17.15 | **B81** | 103.66 | 105.5 | 107.46 |
| **B31** | 17.15 | 17.5 | 17.78 | **B82** | 107.46 | 109.4 | 111.40 |
| **B32** | 17.78 | 18.1 | 18.43 | **B83** | 111.40 | 113.4 | 115.48 |
| **B33** | 18.43 | 18.8 | 19.11 | **B84** | 115.48 | 117.6 | 119.71 |
| **B34** | 19.11 | 19.5 | 19.81 | **B85** | 119.71 | 121.9 | 124.09 |
| **B35** | 19.81 | 20.2 | 20.54 | **B86** | 124.09 | 126.3 | 128.64 |
| **B36** | 20.54 | 20.9 | 21.29 | **B87** | 128.64 | 131 | 133.35 |
| **B37** | 21.29 | 21.7 | 22.07 | **B88** | 133.35 | 135.8 | 138.24 |
| **B38** | 22.07 | 22.5 | 22.88 | **B89** | 138.24 | 140.7 | 143.30 |
| **B39** | 22.88 | 23.3 | 23.71 | **B90** | 143.30 | 145.9 | 148.55 |
| **B40** | 23.71 | 24.1 | 24.58 | **B91** | 148.55 | 151.2 | 153.99 |
| **B41** | 24.58 | 25 | 25.48 | **B92** | 153.99 | 156.8 | 159.63 |
| **B42** | 25.48 | 25.9 | 26.42 | **B93** | 159.63 | 162.5 | 165.48 |
| **B43** | 26.42 | 26.9 | 27.38 | **B94** | 165.48 | 168.5 | 171.54 |
| **B44** | 27.38 | 27.9 | 28.39 | **B95** | 171.54 | 174.7 | 177.83 |
| **B45** | 28.39 | 28.9 | 29.43 | **B96** | 177.83 | 181.1 | 184.34 |
| **B46** | 29.43 | 30 | 30.51 | **B97** | 184.34 | 187.7 | 191.10 |
| **B47** | 30.51 | 31.1 | 31.62 | **B98** | 191.10 | 194.6 | 198.10 |
| **B48** | 31.62 | 32.2 | 32.78 | **B99** | 198.10 | 201.7 | 205.35 |
| **B49** | 32.78 | 33.4 | 33.98 | **B100** | 205.35 | 209.1 | 212.87 |
| **B50** | 33.98 | 34.6 | 35.23 | **B101** | 212.87 | 216.7 | 220.67 |
| **B51** | 35.23 | 35.9 | 36.52 | **B102** | 220.67 | 224.7 | 228.76 |

## A.3. Supplemental Gravimetric PM Data

Gravimetric PM samples were collected with the same engine, dilution system/conditions, and data acquisition system as described above for a transient drive cycle with the engine fueled by blends of ULSD and biodiesel for two feedstocks: waste vegetable oil (WVO) and soybean biodiesel. Figure A.3 shows the average mass concentrations, with one standard deviation, for triplicate tests conducted under each condition.

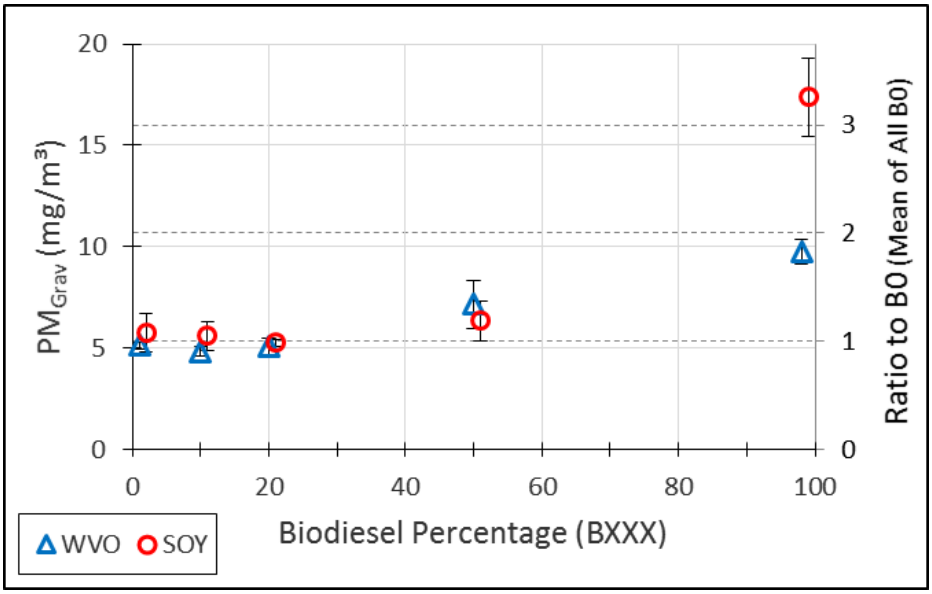


**Figure A.3: Average gravimetric PM (±σ) by biodiesel blend percent**